Sensitivity to local imperfections in inelastic thin-walled rectangular hollow section struts

Jiajia Shen, M. Ahmer Wadee*

Department of Civil and Environmental Engineering, Imperial College London, South Kensington Campus, London SW7 2AZ, UK

Abstract

Mass efficient inelastic thin-walled rectangular hollow section (RHS) struts practically always fail in a combination of local–global interactive buckling and material nonlinearity while also exhibiting high sensitivity to initial imperfections. Nonlinear finite element (FE) models for inelastic thin-walled RHS struts with pre-defined local and global geometric imperfections are developed within the commercial package ABAQUS. Using a unified local imperfection measurement based on equal local bending energy, the effects of imperfect cross-section profiles, imperfection wavelength and the degree of localization in the longitudinal direction on the ultimate load and the nonlinear equilibrium path are investigated for four characteristic length struts at different material yielding stress levels. The corresponding most severe imperfection profiles are determined and are found to be qualitatively different to the linear eigenmodes in all cases. Moreover, it is found that the most severe purely periodic imperfections may be used to provide a safe approximation of the ultimate load when the corresponding amplitude is constrained to the manufacturing tolerance level. An extensive parametric study on the wavelength of the most severe periodic imperfection profile is conducted and a relationship for this is proposed in terms of the normalized local slenderness, which compares excellently with the FE results.

Keywords: Imperfection sensitivity; Mode interaction; Local buckling; Global buckling; Imperfection modelling; Most severe imperfection

1. Introduction

With the development of material science and manufacturing technology alongside fundamentally better understanding of nonlinear mechanics, structural forms have become increasingly slender [1]. Well-known for mass efficiency and the ease of forming into a variety of different profiles, thin-walled structural members are widely used in structural engineering [2, 3]. Buckling instability is practically always the governing failure mode

*Corresponding author

Email addresses: j.shen14@imperial.ac.uk (Jiajia Shen), a.wadee@imperial.ac.uk (M. Ahmer Wadee)

of such members. Moreover, optimized thin-walled members are generally susceptible to triggering different buckling modes simultaneously [4] and exhibit highly nonlinear behaviour with failure modes being associated with a severe degree of sensitivity to imperfections [5, 6, 7, 8, 9, 10]. Moreover, owing to their excellent ductility, most steel thin-walled members in structural engineering are designed such that their ultimate state lies in the elasto-plastic range [11], which has also been observed in many experimental studies [12, 13, 14, 15, 16, 17]. The coupling of material nonlinearity and buckling mode interaction has been shown to increase the imperfection sensitivity further [18, 19]. The erosion in the load-carrying capacity may be up to 50% for members with tolerance level geometric imperfections [20]. Therefore, the treatment of geometric imperfections is of great importance in such members since it affects both the ultimate load and the post-buckling behaviour.

Owing to its modelling convenience, the introduction of local geometric imperfections affine to the local eigenmode (or modes) with the lowest load that can trigger the ultimate failure mode is still one of the most widely accepted methodologies in both research and design practice [21, 22, 23, 19]. However, actual geometric imperfections are affected by a great many factors, *e.g.* material and cross-section properties, manufacturing methods and handling [24]. They are essentially random variables and measured imperfection data have demonstrated that they are far removed from the linear buckling modes [25, 26, 16]. More importantly, several studies have demonstrated that the local eigenmode with the lowest load may not even represent the most severe imperfection profile anyway [27, 28, 29, 30, 31].

Much effort has been devoted to developing the methodology for determining geometric imperfections that reflect those in physical reality by expanding the imperfection profiles from the space of linear buckling modes using statistical methods [32, 33]. These methods can generally provide reasonably accurate predictions for the ultimate load alongside the final failure mechanism. However, since imperfections are essentially stochastic quantities, a large number of analyses are required to obtain statistically significant results [34].

Since localized imperfections are very common in practice, arising for instance from component joining processes or mishandling, a series of investigations on the effects of localized imperfections on the ultimate load and failure mechanism of plates under pure compression have been conducted [35, 36, 37]. It has been determined that localized imperfections have minor effects on the stiffness of plates but may lead ultimately to a violent collapse, *i.e.* a sharp unloading being observed beyond the ultimate state. Moreover, effects of localized imperfections on the ultimate strength have been found to be negligible for stocky plates but significant for slender ones. The effect of these localized imperfections was mainly determined by their amplitude while the shape and position along the plate length was shown not to have a major influence. However, these works were only limited to a single plate or panel. A systematic study is therefore required to understand the behaviour in plate assemblies, which are also more susceptible to nonlinear buckling mode interaction.

Recently, the authors investigated the imperfection sensitivity of elastic and inelastic thin-walled rectangular hollow section (RHS) struts using variational [38] and finite element (FE) models [20, 39] respectively. The sensitivity to local imperfections, global imperfec-

tions as well as their combinations for struts with different slenderness levels was quantified and the underlying mechanism was explained. In particular, a unified local imperfection measurement method, based on an equivalent local bending energy of the initial imperfect geometry, was proposed to investigate the effects of local imperfection profiles on the erosion in the load-carrying capacity for purely elastic struts. It revealed that the wavelength of the most severe local imperfection profile is significantly smaller than that of the local eigenmode with the smallest load. Moreover, introducing a modulated amplitude in the local imperfection profile leads to a further decrease in the ultimate load. However, struts with highly localized local imperfection profiles exhibited a relatively stiffer response, thus leading to a higher ultimate load, which implies that there exists a 'most severe' profile.

The current article is related to the work presented in [20] but with an increased focus on the effects of material nonlinearity. A validated nonlinear FE model with pre-defined geometric imperfections developed within the commercial package ABAQUS is adopted [39]. Based on the aforementioned unified geometric imperfection measurement [20], the effects of imperfection profiles, *i.e.* the cross-section profile, the longitudinal wavelength and the degree of localization, on the ultimate load of four characteristic length struts with different yielding stress levels are investigated. The most severe local imperfection profiles are identified and the underlying failure mechanism of struts with different periodic and localized imperfection profiles are also discussed. Even though the localized imperfections are consistently found to be the most severe particularly for struts with lower local slenderness levels, it is also determined that the ultimate load can be approximately minimized with the purely periodic imperfection where the amplitude is constrained to the manufacturing tolerance. Hence, a simplified equation to determine the wavelength of the most severe periodic imperfection profile is proposed from a parametric study. The current work provides a better understanding of the effects of different local imperfection profiles on the load-carrying capacity of inelastic thin-walled RHS struts and presents a more rational local imperfection modelling approach that can be implemented in nonlinear FE analyses.

2. Development of finite element model

A thin-walled rectangular hollow section (RHS) strut of length L with simply-supported boundary conditions under an axial load P is considered, as shown in Figure 1(a, b). The web depth and flange width are d and b respectively; the web and flange thicknesses are assumed to be uniform and are labelled as t. The joints between the flanges and webs are assumed to be rigid. The FE model is developed within the general-purpose package ABAQUS [40]. It should be noted that the geometric and material nonlinear FE model with the same properties has been developed in [20, 39]. Therefore, only a brief overview of the FE model is provided currently.

2.1. Strut modelling

Based on previous work [41], the FE model exploits two planes of symmetry for computational efficiency, as shown in Figure 1(c). A reference point, as well as rigid body coupling, is introduced at the loaded-end section to ensure that the pinned-roller support

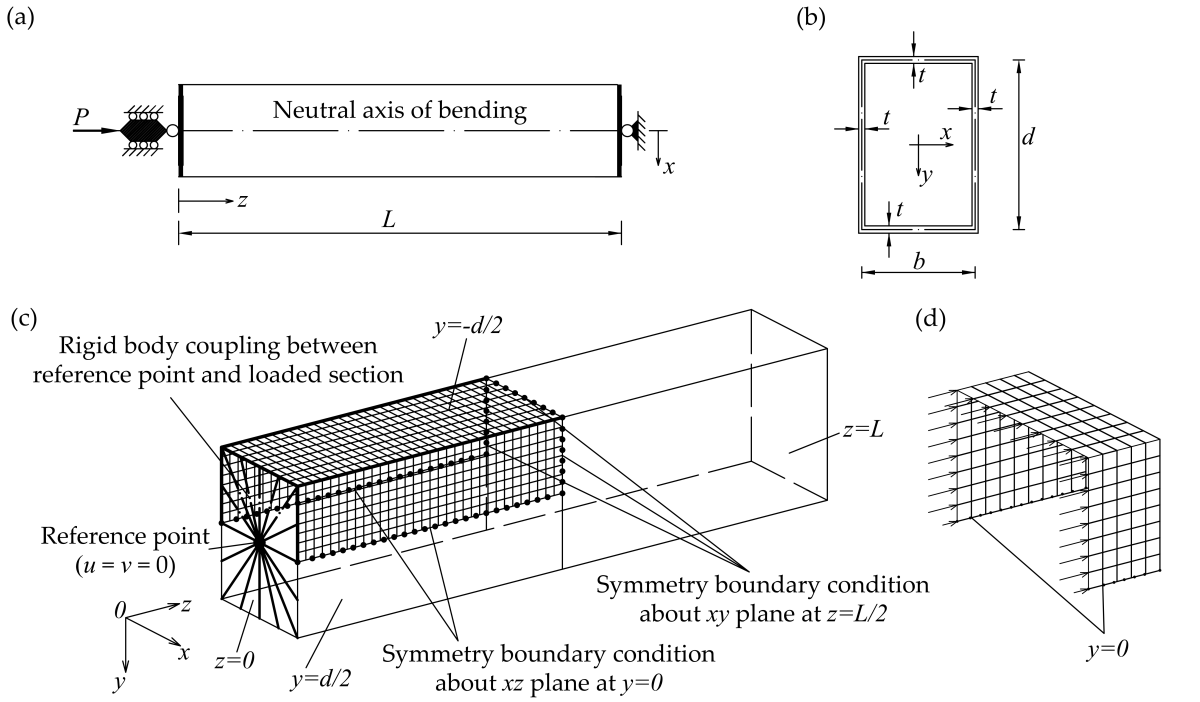

Figure 1: Geometric properties of the thin-walled RHS strut and the illustration of the FE model. (a) Plan view of the strut of length L under an axial load P. Lateral and longitudinal coordinates are x and z respectively. (b) Cross-section properties of the strut; the vertical coordinate being y. (c) Illustration of the FE model for thin-walled RHS struts. Global buckling bends the strut about the weak axis y. (d) Distributed applied load at the end-section: magnitude of the load on the nodes at the symmetric line ($y = 0$) is half of that applied to the other nodes.

condition is satisfied. In terms of the axial load, it is applied as a distributive load on each node at the end-section, as shown in Figure 1(d). In particular, the magnitude of the applied load on the two nodes at the symmetric line ($y = 0$) is one-half of those on the other nodes. It should be noted that this choice of doubly-symmetry and load application was made after careful verification against the full models [41]. As for the element type, 4-node reduced-integration S4R general-purpose shell elements were selected, which have been demonstrated to be capable of modelling the nonlinear geometric and material behaviour of plated structures with very good accuracy [42, 23, 15]. The element size was kept to be one-tenth of the local eigenmode (*i.e.* the linear local buckling mode) half-wavelength in the longitudinal direction [20], which has been demonstrated to produce more than satisfactory results while maintaining computational efficiency [43].

The material is assumed to be homogeneous and isotropic with Young's modulus E, Poisson's ratio ν and shear modulus $G = E/[2(1 + \nu)]$. Previous studies [44, 39] have demonstrated that the material strain-hardening rate of 2%, which is the typical value for structural carbon steel [45, 46], has a negligible effect on the ultimate load of thin-walled box-section struts susceptible to local–global mode interaction. Therefore, an elastic–

perfectly plastic model was adopted. Full details of the strut modelling may be found in [20].

2.2. Geometric imperfection description and modelling

Rather than using the keyword '*IMPERFECTION' in ABAQUS to introduce the shape of the eigenmodes from linear buckling analysis (LBA) as geometric imperfections, a pre-processing program was developed in MATLAB to generate the nodal coordinates input file for the FE model with pre-defined global or local imperfections. The local and global imperfections are based on the descriptions of the local and global buckling modes presented in [47, 41, 20], which have been demonstrated to be capable of describing purely local and global buckling modes as well as the interactive post-buckling mode very well. As for the global imperfection, it is decomposed into two components, an initial out-of-straightness in the x-direction W_0 and an initial pure rotation of the plane section θ_0, as shown in Figure 2(a), which are known as the 'sway' and 'tilt' modes respectively [48]. They are

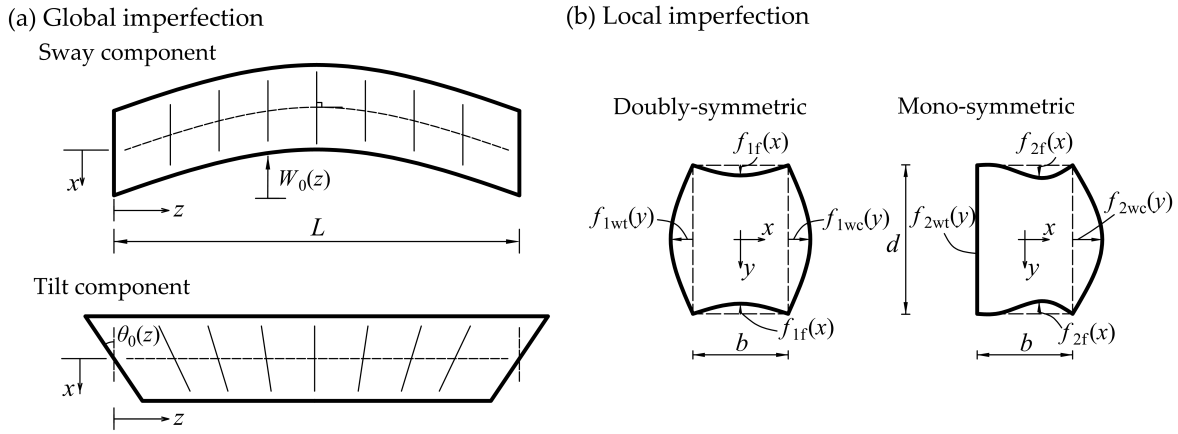

Figure 2: Imperfection descriptions. (a) Global imperfection bending about the weak axis y: sway and tilt components. (b) Cross-section component of local imperfections: doubly-symmetric and mono-symmetric profiles.

defined by the following expressions:

$$W_0(z) = -q_{s0} L \sin\left(\frac{\pi z}{L}\right), \quad \theta_0(z) = -q_{t0}\pi \cos\left(\frac{\pi z}{L}\right), \tag{1}$$

with q_{s0} and q_{t0} being the respective normalized amplitudes. Moreover, previous work [38] has demonstrated that the following relationship for q_{s0} and q_{t0} should be satisfied for compatibility:

$$q_{s0} = (1+s)\, q_{t0}, \tag{2}$$

where s is the shear correction factor, thus:

$$s = \frac{\pi^2 E b^2}{12 G L^2}(1 + 3\phi_c), \tag{3}$$

with $\phi_c = d/b$ being the cross-section aspect ratio.

With the similar approach adopted in previous studies [49, 30, 50, 31, 38], the local imperfection is introduced by defining an initial out-of-plane deflection in both flanges and webs, which has the same format as the local eigenmode description in [41]:

$$\begin{aligned} w_{\mathrm{f0}}(x,z) &= f_{1\mathrm{f}}(x)w_{10}(z) + f_{2\mathrm{f}}(x)w_{20}(z), \\ w_{\mathrm{wc0}}(y,z) &= f_{1\mathrm{wc}}(y)w_{10}(z) + f_{2\mathrm{wc}}(y)w_{20}(z), \\ w_{\mathrm{wt0}}(y,z) &= f_{1\mathrm{wt}}(y)w_{10}(z) + f_{2\mathrm{wt}}(y)w_{20}(z), \end{aligned} \tag{4}$$

where f represents the cross-sectional components of the local imperfection, as shown in Figure 2(b); w_{i0}, where $i = \{1, 2\}$, are the longitudinal components. Subscripts 1 and 2 represent the doubly-symmetric and mono-symmetric cross-sectional profiles respectively, as shown in Figure 2(b), which correspond to the purely local buckling and globally induced interactive post-buckling modes respectively [41]. They are approximated by applying kinematic and static boundary conditions for each plate at their joints in conjunction with the Rayleigh–Ritz method:

$$\begin{aligned} f_{1\mathrm{wc}} &= \frac{C_{1\mathrm{w}}}{C_{10}}\cos\frac{\pi y}{d} + \left(1 - \frac{C_{1\mathrm{w}}}{C_{10}}\right)\left(1 - \frac{4y^2}{d}\right), \\ f_{1\mathrm{f}} &= \frac{C_{1\mathrm{f1}}}{C_{10}}\left(1 - \frac{4x^2}{b}\right) + \frac{C_{1\mathrm{f2}}}{C_{10}}\cos\frac{\pi x}{b}, \\ f_{2\mathrm{wc}} &= \frac{C_{2\mathrm{w}}}{C_{20}}\cos\frac{\pi y}{d} + \left(1 - \frac{C_{2\mathrm{w}}}{C_{20}}\right)\left(1 - \frac{4y^2}{d^2}\right), \\ f_{2\mathrm{f}} &= \frac{C_{2\mathrm{f}}}{C_{20}}\left(\frac{x}{b} + \frac{1}{2}\right)^2\left(\frac{x}{b} - \frac{1}{2}\right), \quad f_{2\mathrm{wt}} = 0, \end{aligned} \tag{5}$$

where:

$$\begin{aligned} C_{1\mathrm{w}} &= 214.60 + 679.81\phi_c - 1158.10\phi_c^2 + 92\phi_c^3, \\ C_{1\mathrm{f1}} &= \pi\left(250/\phi_c - 273 + 23\phi_c\right), \\ C_{1\mathrm{f2}} &= -785.40/\phi_c + 771.81 - 158.10\phi_c, \\ C_{2\mathrm{w}} &= -2\left(2\phi_c + 1\right), \\ C_{2\mathrm{f}} &= -2\pi/\phi_c, \\ C_{10} &= 214.60 - 105.58\phi_c - 300.45\phi_c^2 + 19.74\phi_c^3, \\ C_{20} &= \pi\phi_c - 4\phi_c - 2. \end{aligned} \tag{6}$$

The detailed derivations of Eqs. (5) and (6) as well as their verification against FE results may be found in [20, 47].

The longitudinal component of the local imperfection $w_{i0}(z)$ is derived from a first-order approximation of a multiple scale perturbation analysis of a strut on a nonlinear softening foundation [51], which has also been used to investigate the most severe imperfection profile in sandwich panels [49], I-section struts [30, 31], stiffened plates [50] and functionally-

graded carbon nanotube-reinforced composite beams [52]:

$$w_{i0}(z) = A_{i0}\,\mathrm{sech}\left[\alpha_i\left(\frac{z}{L}-\frac{1}{2}\right)\right]\cos\left[\beta_i\pi\left(\frac{z}{L}-\frac{1}{2}\right)\right], \tag{7}$$

where $z = [0, L]$ and the imperfection is symmetric about $z = L/2$; the quantity A_{i0} controls the imperfection amplitude; parameters α_i and β_i control the degree of localization of the imperfection and its number of half-waves respectively, as shown in Figure 3. It should be

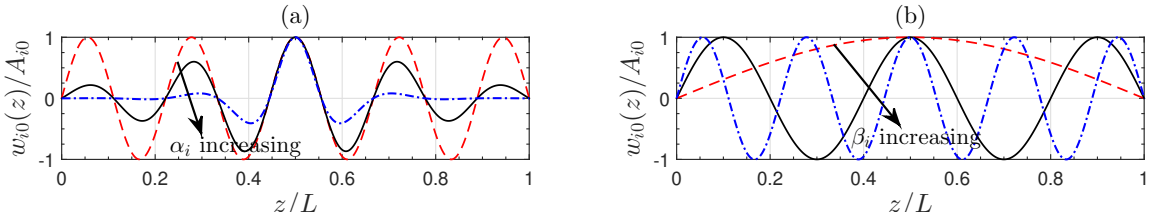

Figure 3: Profile of the local imperfection function, $w_{i0}(z)/A_{i0}$. (a) Localized imperfections introduced by varying the localization parameter α_i from zero to 10. (b) Periodic imperfections ($\alpha_i = 0$) with different numbers of half sine waves by varying the frequency parameter β_i from 1 to 9.

noted that β_i should be an odd number such that the boundary conditions at the strut ends are satisfied. The wavelength of the longitudinal component of the local imperfection is defined as $\Lambda = 2L/\beta_i$.

2.3. Solution strategy and validation

The Riks arc-length method [53] is used to trace the nonlinear equilibrium path of imperfect struts. In the parametric studies where only the ultimate load is of interest, a function developed in MATLAB, which can monitor the nonlinear Riks arc-length analysis and terminate it automatically once certain failure criteria are met, is adopted. This greatly improves the computational efficiency in the search of the most severe imperfection profile. Further details about the function may be found in [39].

The developed FE model has been validated against experimental results from two independent sources [54, 16]; very good comparisons have been observed for both ultimate loads and equilibrium paths, the details of which may be found in [39].

3. Unified local imperfection measurement criterion

Since there are many varying parameters in the imperfections investigated, *i.e.* the imperfection amplitude A_{i0}, the number of half-waves in the longitudinal direction β_i, the degree of localization α_i and the cross-section profile functions f, purely using the imperfection amplitude A_{i0} as the sole measurement of imperfection inevitably neglects important features and hinders meaningful comparisons being made. Even though the fundamentally one-dimensional approach based on the concept of the initial total end-shortening due to local imperfections [49, 30] considers the contributions from all parameters in Eq. (7), *i.e.* the

variation of the local imperfection in the longitudinal direction, it is not easily adaptable for providing the comparison between the doubly-symmetric and mono-symmetric cross-section imperfection profiles in the current case. Therefore, an imperfection measurement approach based on the initial local bending energy is adopted currently. It should be noted that similar approaches have also been adopted previously in investigations on the effects of local imperfection profiles in the response of simply-supported rectangular plates [36] and the imperfection sensitivity of lipped channel columns [55]. From classical plate bending theory [56], the generalized expression for local bending energy due to initial imperfections in each plate $U^0_{\mathrm{b,lp}}$ can be expressed thus:

$$U^0_{\mathrm{b,lp}} = \frac{D_{\mathrm{p}}}{2}\int_0^L \int_{-b_{\mathrm{p}}/2}^{b_{\mathrm{p}}/2} \left\{ \left(\frac{\partial^2 w_{\mathrm{p0}}}{\partial z^2} + \frac{\partial^2 w_{\mathrm{p0}}}{\partial x_{\mathrm{b}}^2} \right)^2 - 2(1-\nu)\left[\frac{\partial^2 w_{\mathrm{wc0}}}{\partial z^2}\frac{\partial^2 w_{\mathrm{p0}}}{\partial x_{\mathrm{b}}^2} - \left(\frac{\partial^2 w_{\mathrm{p0}}}{\partial z \partial x_{\mathrm{b}}} \right)^2 \right] \right\} \mathrm{d}x_{\mathrm{b}}\,\mathrm{d}z, \tag{8}$$

where $D_{\mathrm{p}} = Et^3/\left[12(1-\nu^2)\right]$ is the plate flexural rigidity; L and b_{p} are the plate length and width respectively; w_{p0} is the initial out-of-plane displacement of the plate; z and x_{b} are the longitudinal and transverse coordinates of the plate respectively. Based on previous studies regarding the energy formulation of thin-walled RHS struts [41], the total local bending energy stored in the entire strut due to the initial local imperfections $U^0_{\mathrm{b,l}}$ can be expressed thus:

$$U^0_{\mathrm{b,l}} = U^0_{\mathrm{b,lf}} + U^0_{\mathrm{b,lwc}} + U^0_{\mathrm{b,lwt}}, \tag{9}$$

where $U^0_{\mathrm{b,lf}}$, $U^0_{\mathrm{b,lwc}}$, $U^0_{\mathrm{b,lwt}}$ are the local bending energies due to the initial local imperfections in both flanges, the more compressed web and the less compressed web respectively.

By substituting w_{f0}, w_{wc0} and w_{wt0} from Eq. (4) into Eq. (9), the local bending energy due to the initial local imperfections with the doubly-symmetric ($i = 1$) and mono-symmetric ($i = 2$) cross-sectional components can be expressed thus:

$$\begin{aligned} U^0_{\mathrm{b,l}i} = D_{\mathrm{p}}\int_0^L \Bigg[& \left(2\left\{ f_{i\mathrm{f}}^2 \right\}_x + \left\{ f_{i\mathrm{wc}}^2 \right\}_y + \left\{ f_{i\mathrm{wt}}^2 \right\}_y \right) \ddot{w}_{i0}^2 \\ & + \left(2\left\{ f_{i\mathrm{f}}''^2 \right\}_x + \left\{ f_{i\mathrm{wc}}''^2 \right\}_y + \left\{ f_{i\mathrm{wt}}''^2 \right\}_y \right) w_{i0}^2 \\ & + 2\nu \left(2\left\{ f_{i\mathrm{f}} f_{i\mathrm{f}}'' \right\}_x + \left\{ f_{i\mathrm{wc}} f_{i\mathrm{wc}}'' \right\}_y + \left\{ f_{i\mathrm{wt}} f_{i\mathrm{wt}}'' \right\}_y \right) \ddot{w}_{i0} w_{i0} \\ & + 2\left(1-\nu\right) \left(2\left\{ f_{i\mathrm{f}}'^2 \right\}_x + \left\{ f_{i\mathrm{wc}}'^2 \right\}_y + \left\{ f_{i\mathrm{wt}}'^2 \right\}_y \right) \dot{w}_{i0}^2 \Bigg] \mathrm{d}z, \end{aligned} \tag{10}$$

where dots represent differentiation with respect to z; primes denote differentiation with respect to x and y for the flanges and webs respectively; the terms $\{X\}_x$ and $\{Y\}_y$ represent

definite integrals with respect to their corresponding subscript, thus:

$$\{X\}_x = \int_{-b/2}^{b/2} X \, \mathrm{d}x, \quad \{Y\}_y = \int_{-d/2}^{d/2} Y \, \mathrm{d}y. \tag{11}$$

From Eqs. (9) and (10), it can be seen that the variation of local imperfections in both the cross-sectional and longitudinal dimensions can be considered. Moreover, the advance in imperfection measurement facilities [57] has made it possible to obtain the three-dimensional distribution of local imperfections. Using numerical integration, the corresponding local bending energy can be obtained, which can be adopted as the reference value to compare different imperfection profiles.

3.1. Algorithm determining most severe local imperfection

The investigation to determine the most severe local imperfections comprises two stages, as shown in Figure 4:

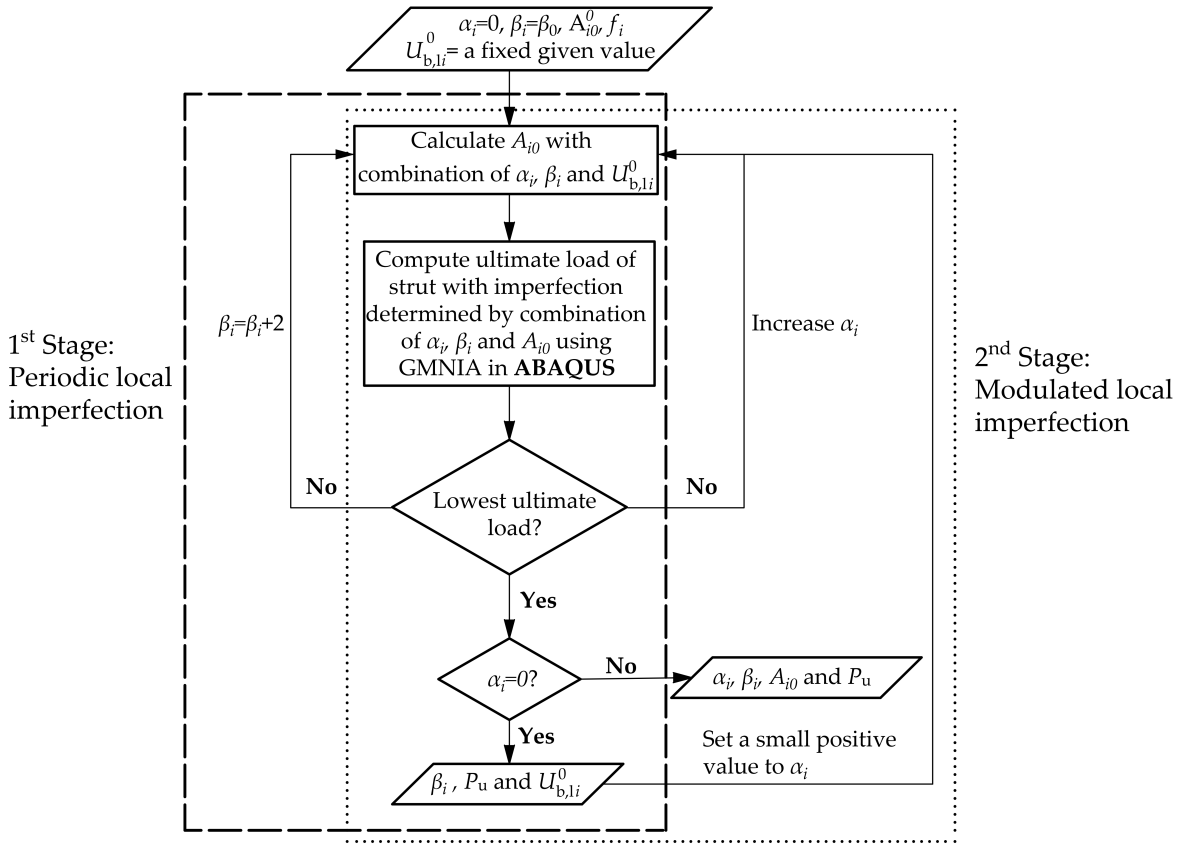

Figure 4: Algorithm for determining the most severe periodic and modulated local geometric imperfections under the constraint of the equal local bending energy of the initially imperfect geometry.

1. Periodic imperfections are investigated by adopting β_i as the principally varying parameter. Initially, the value of $U^0_{\mathrm{b,l}i}$ is determined and fixed based on the combination of $\alpha_i = 0$, β_i being the number of half waves of the purely local eigenmode β_{i0} from the analytical model [41], and A^0_{i0} being the local imperfection amplitude tolerance level value adopted from Eurocode 3 [58]. Then, the quantity β_i is varied as the principal parameter and increased from a sufficiently small, but reasonable, odd integer while the value of α_i remains precisely zero. Note that the value of β_i only takes odd integer values such that the boundary conditions are satisfied. The amplitude A_{i0} is varied accordingly to keep $U^0_{\mathrm{b,l}i}$ at the selected value; hence, increasing β_i would naturally lead to a decrease in A_{i0}. Geometrically and Material Nonlinear Analysis with Imperfections (GMNIA) is conducted to obtain the ultimate load of the strut with each combination of β_i and A_{i0}. In particular, the combination of β_i and A_{i0} that gives the lowest ultimate load P_{u} is recorded and used for the modulated imperfection study.
2. Modulated local imperfections are investigated by adopting α_i as the principally varying parameter. The quantities β_i and $U^0_{\mathrm{b,l}i}$ are the same as those corresponding to the lowest ultimate load in stage 1. The localization parameter α_i is set as the principal varying parameter and the amplitude A_{i0} is varied accordingly to keep $U^0_{\mathrm{b,l}i}$ constant; increasing α_i naturally leads to a higher value of A_{i0}. GMNIA is also conducted to obtain the ultimate load of the strut with each imperfection combination of α_i and A_{i0}. In particular, the combination of α_i and A_{i0} that gives the lowest ultimate load P_{u} is recorded.

4. Numerical results

A previous study [41] has demonstrated that there are four distinct length-related zones for thin-walled RHS struts, which exhibit characteristic interactive buckling behaviour, as shown in Figure 5. Therefore, four struts with the same cross-section properties but different characteristic lengths are selected, which are the same as those presented in [41, 20]. The material and cross-section properties of the example struts are presented in Table 1. Strut lengths, the global and local buckling loads, the number of half-waves of

Table 1: Material and cross-section properties of the example thin-walled RHS struts in the numerical examples.

Young's Modulus E	Poisson's ratio ν	Flange width b	Web depth d	Plate thickness t
210 kN/mm^2	0.3	60 mm	120 mm	1 mm

the local eigenmode with the lowest load β_0 and corresponding zones of the example struts are summarized in Table 2.

For each characteristic length strut, four different imperfection cases are studied, as presented in Table 3. For the first case, the imperfection profile is the local eigenmode with the lowest load obtained from linear buckling analysis using the FE model and the

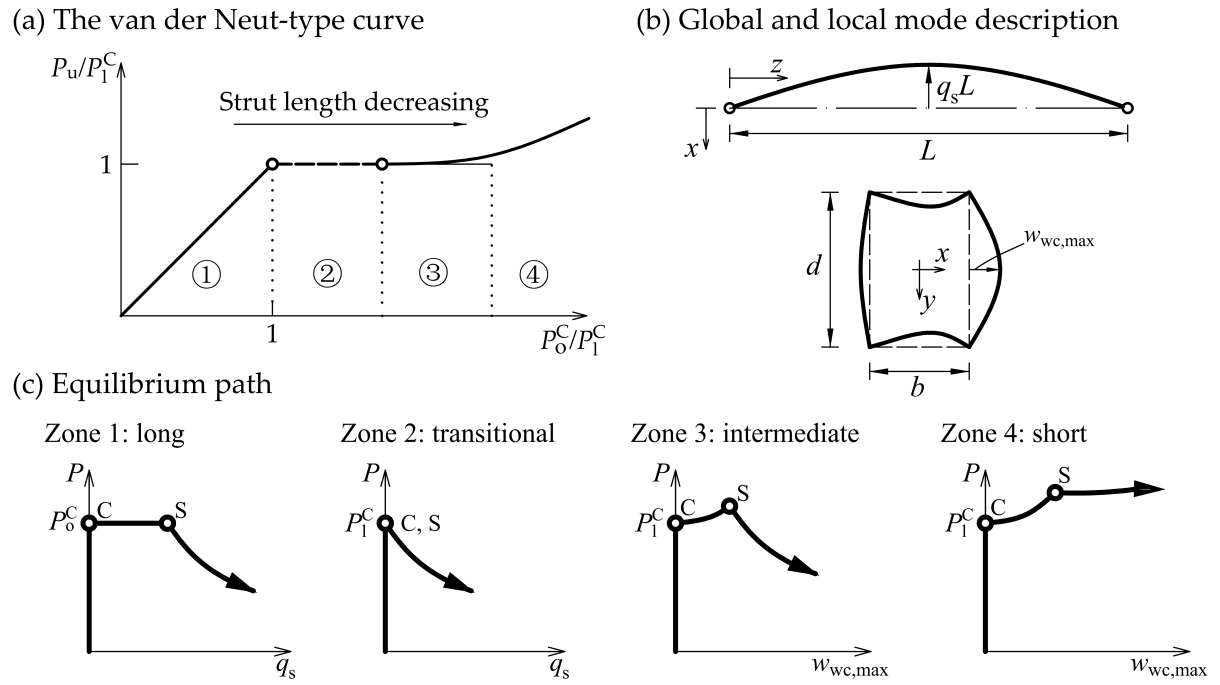

Figure 5: (a) Van der Neut-type curve [21] for perfect thin-walled RHS struts with P_{u}, $P_{\mathrm{l}}^{\mathrm{C}}$ and $P_{\mathrm{o}}^{\mathrm{C}}$ being the ultimate, local buckling and global buckling loads respectively. (b) Global buckling mode bending about the weak axis y with the deflection at mid-span being $q_{\mathrm{s}}L$; cross-section profile of the interactive post-buckling mode at mid-span with the maximum out-of-plane displacement in the more compressed web being $w_{\mathrm{wc,max}}$. (c) Sketches of equilibrium paths for struts corresponding to zones 1–4 as presented in (a). Circles marked C and S represent the critical and secondary bifurcation points for each case respectively. Note that the abscissa changes from the normalized global amplitude q_{s} for struts in zones 1 and 2 to $w_{\mathrm{wc,max}}$ for those in zones 3 and 4, reflecting the primary buckling mode amplitude. Note also that the Van der Neut-type relationship in zones 3 and 4 is curved owing to the strut tangent stiffness decreasing with the advance of local buckling.

corresponding imperfection amplitude is $d/200$, which is the tolerance level for the local imperfection amplitude, as recommended by Eurocode 3 [58]. It is used as a reference to compare with the imperfection profiles in other cases. The second case adopts the mono-symmetric cross-section imperfection profile, with the number of half-waves along the strut length β_0 being equal to those listed in Table 2 and the initial imperfection amplitude A_{i0}^0 also being $d/200$. The third case adopts the doubly-symmetric cross-section imperfection profile and the local bending energy due to local imperfections is equal to that in the second case, which aims to study the more severe case between the mono-symmetric and doubly-symmetric ones with the same local bending energy stored from the initially imperfect geometry. The fourth case adopts the doubly-symmetric cross-section imperfection profile, with β_0 and A_{i0}^0 being the same as those in the second case; this aims to study the more severe case between the mono-symmetric and doubly-symmetric cases with the same local imperfection amplitude. Note that β_i and A_{i0} are subsequently varied from β_0 and A_{i0}^0, which are only the starting values to establish $U_{\mathrm{b,l}i}^0$, in accordance with the algorithm

Table 2: Theoretical values of the global and local critical buckling loads and the number of half-waves β_0 in the local eigenmode with the lowest load for the four characteristic length cases [41]. Note that the detailed expressions to determine the values of $P_{\mathrm{o}}^{\mathrm{C}}$, $P_{\mathrm{l}}^{\mathrm{C}}$ and β_0 may be found in [41, 20].

L(mm)	$P_{\mathrm{o}}^{\mathrm{C}}$ (kN)	$P_{\mathrm{l}}^{\mathrm{C}}$ (kN)	β_0	$P_{\mathrm{o}}^{\mathrm{C}}/P_{\mathrm{l}}^{\mathrm{C}}$	Zone	Length description
4800	22.67	24.50	49	0.92	1	'Long'
4500	25.79	24.49	45	1.05	2	'Transitional'
4000	32.54	24.50	41	1.32	3	'Intermediate'
3600	40.30	24.51	37	1.63	4	'Short'

Table 3: Initial local imperfection parameters for the most severe local imperfection case study. Note that 'Eval' represents quantities evaluated based on the other input parameters and the number of half-waves of the local imperfection in each case β_i=β_0 at the beginning of the parametric study.

Case	$U_{\mathrm{b,l}i}^0$	A_{i0}^0	Cross-section profile f_i	Notes
1	N/A	$d/200$	doubly-symmetric	Linear buckling mode
2	$U_{\mathrm{b,l2}}^0$	$d/200$	mono-symmetric	A_{10}^0=0, A_{20}^0=$d/200$
3	$U_{\mathrm{b,l2}}^0$	Eval	doubly-symmetric	$U_{\mathrm{b,l}}^0$ is equal to that in case 2
4	Eval	$d/200$	doubly-symmetric	A_{10}^0=$d/200$, A_{20}^0=0

presented in Figure 4. Moreover, the global imperfection with the normalized amplitude q_{s0}=10^{-3} is introduced in all example struts, which is the recommended value for ultimate load prediction purposes in Eurocode 3 [59].

4.1. Effects of varying number of sinusoidal half-waves β_i

The normalized ultimate loads of struts with various different local periodic imperfection profiles at different material yielding stress levels are shown in Figure 6. In particular, four typical yielding stress levels are selected, *i.e.* $P_{\mathrm{y}}/P_{\mathrm{l}}^{\mathrm{C}} = \{1, 1.5, 2, 4\}$ and the corresponding normalized local slendernesses $\bar{\lambda}_{\mathrm{p}} = \sqrt{P_{\mathrm{y}}/P_{\mathrm{l}}^{\mathrm{C}}} = \{1, 1.225, 1.414, 2\}$, with P_{y} and $P_{\mathrm{l}}^{\mathrm{C}}$ being the the squash load evaluated in conjunction with the gross cross-sectional area and the local buckling load respectively [2]. With the increase of the number of half-waves β_i, the normalized ultimate load $p_{\mathrm{u}} = P_{\mathrm{u}}/P^{\mathrm{C}}$, where P^{C} is the critical buckling load of the perfect strut, decreases and then increases again. This trend is the same as that for the purely elastic case [20]. It should be noted that under the equal local bending energy constraint, the imperfection amplitude naturally decreases with increasing β_i. Therefore, it is confirmed that the imperfection amplitude itself only cannot be used as the unique measure for determining the severity of the different imperfection profiles.

A summary of the most severe imperfection profiles and the corresponding ultimate loads are presented in Table 4. Similar to the purely elastic case, the longitudinal wavelength of the most severe imperfection is significantly smaller than that of the perfect strut in terms of the local eigenmode with the lowest load as well as that of the local–global interactive post-buckling mode, as shown in Figure 6. The corresponding imperfection amplitudes are also smaller than the tolerance level, where $A_0^{\mathrm{Tol}} = d/200 = 0.6t$ currently. For cases 2 and 4, where the initial local imperfection parameters A_{i0}^0 and β_i^0 are the same

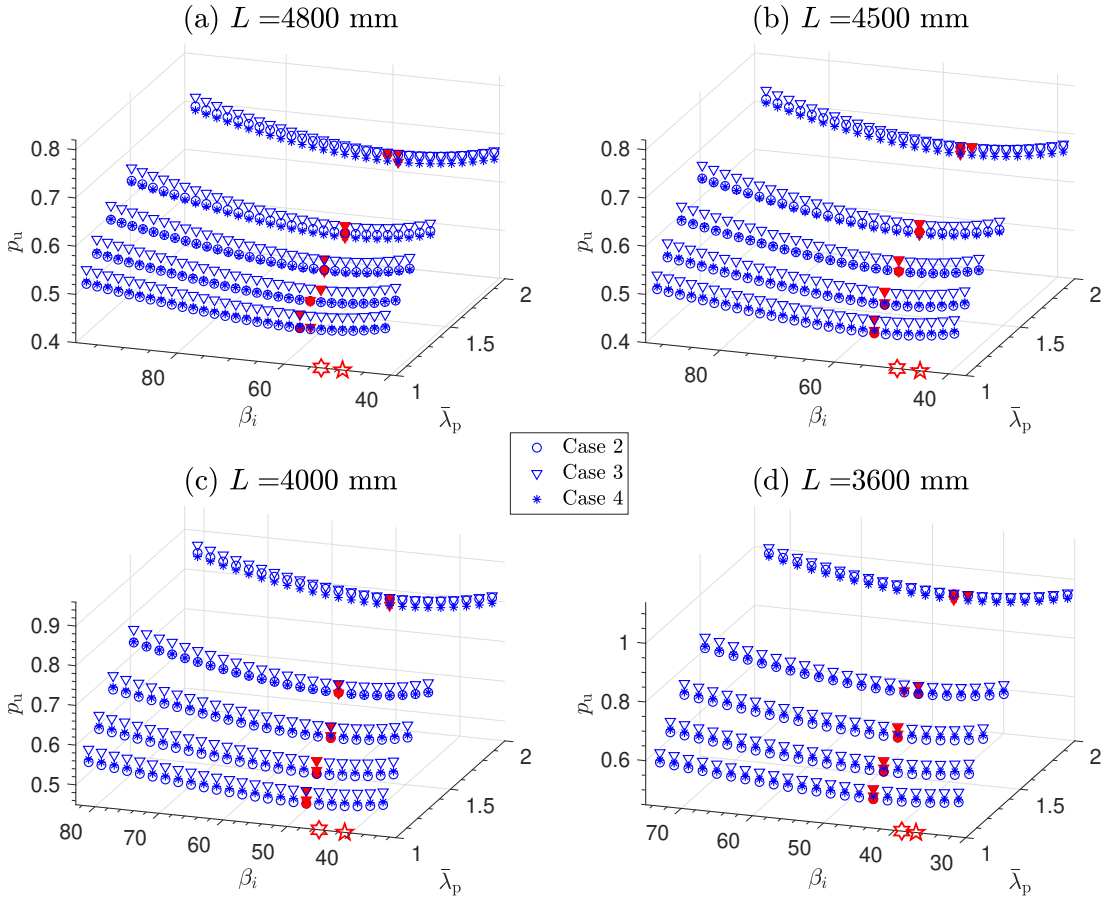

Figure 6: Normalized ultimate load $p_u = P_u/P^C$ versus number of half-waves β_i with different local imperfection cases presented in Table 3 for different length struts with different cross-sectional local slenderness levels $\bar{\lambda}_p$. Solid symbols represent the most severe periodic imperfection profile for each case. The pentagram and hexagram on the β_i axis represent the number of half-waves in the purely local eigenmode and in the local–global interactive post-buckling mode of the perfect struts respectively; recall that the interactive post-buckling mode has a naturally modulated amplitude.

as for case 1 (see Table 3), the corresponding ultimate loads are smaller than those of case 1 at all $\bar{\lambda}_p$ levels. The largest difference is up to 8% for the transitional length strut with $L = 4500$ mm, $\bar{\lambda}_p = 1$ and a mono-symmetric imperfection. The difference is even larger if the corresponding imperfection amplitude is scaled to the tolerance level. Therefore, it is also confirmed that the local eigenmode with the lowest load does not necessarily represent the most severe imperfection profile.

For cases 2–4, the most severe periodic imperfection profile varies with the cross-sectional slenderness level $\bar{\lambda}_p$. When $\bar{\lambda}_p$ is large, the most severe imperfection profile corresponds to case 4 for all four characteristic length struts, which is in accord with the purely elastic case [20]. However, with the decrease of $\bar{\lambda}_p$, imperfections with a mono-symmetric cross-section component (case 2) become the most severe case; this change in

Table 4: Normalized ultimate load, local imperfection amplitude and longitudinal wavelength of the most severe local periodic imperfection profile Λ_{Worst} at different local slenderness levels $\bar{\lambda}_{\text{p}}$. Note that ultimate loads (P_{u}) are normalized with respect to case 1 ($P_{\text{u,LBA,FE}}$), where the local eigenmode with the lowest load is introduced as a geometric imperfection with the amplitude being $A_{i0}/t = 0.6$ for all lengths; Λ_{Worst} is normalized with respect to the longitudinal wavelength local eigenmode from case 1, Λ_{LBA}. Also note that the numbers in bold in the ultimate load columns represent the lowest values amongst cases 2 to 4.

L	$\bar{\lambda}_{\text{p}}$	$P_{\text{u}}/P_{\text{u,LBA,FE}}$ cases			A_{0i}/t cases			$\Lambda_{\text{Worst}}/\Lambda_{\text{LBA}}$ cases		
(mm)		2	3	4	2	3	4	2	3	4
	1.000	**0.964**	1.022	0.972	0.514	0.365	0.530	0.860	0.860	0.891
	1.095	**0.967**	1.017	0.970	0.514	0.380	0.508	0.860	0.891	0.860
4800	1.225	0.973	1.012	**0.967**	0.514	0.365	0.508	0.860	0.860	0.860
	1.414	0.980	1.006	**0.966**	0.514	0.365	0.508	0.860	0.860	0.860
	2.000	0.989	0.994	**0.965**	0.475	0.350	0.487	0.803	0.831	0.831
	1.000	**0.912**	0.969	0.924	0.509	0.361	0.502	0.849	0.849	0.849
	1.095	**0.917**	0.967	0.924	0.509	0.361	0.502	0.849	0.849	0.849
4500	1.225	**0.928**	0.968	**0.928**	0.509	0.361	0.502	0.849	0.849	0.849
	1.414	0.944	0.971	**0.935**	0.509	0.361	0.502	0.849	0.849	0.849
	2.000	0.970	0.975	**0.949**	0.468	0.346	0.460	0.789	0.818	0.789
	1.000	**0.956**	1.018	0.974	0.522	0.371	0.516	0.872	0.872	0.872
	1.095	**0.956**	1.013	0.972	0.522	0.371	0.516	0.872	0.872	0.872
4000	1.225	**0.960**	1.006	0.969	0.522	0.371	0.516	0.872	0.872	0.872
	1.414	0.969	1.000	**0.967**	0.498	0.353	0.491	0.837	0.837	0.837
	2.000	0.984	0.988	**0.963**	0.475	0.336	0.468	0.804	0.804	0.804
	1.000	**0.957**	1.017	0.976	0.514	0.365	0.508	0.860	0.860	0.860
	1.095	**0.955**	1.012	0.974	0.514	0.365	0.508	0.860	0.860	0.860
3600	1.225	**0.955**	1.005	0.972	0.514	0.365	0.508	0.860	0.860	0.860
	1.414	**0.962**	0.998	0.969	0.514	0.365	0.481	0.860	0.860	0.822
	2.000	0.982	0.987	**0.964**	0.463	0.345	0.455	0.787	0.822	0.787

the most severe imperfection profile is attributed to the change in the ultimate failure mode. For illustration purposes, the equilibrium paths of long length struts with mono-symmetric and doubly-symmetric imperfections (case 4), where $\bar{\lambda}_{\text{p}} = 1$ and 2, are presented in Figure 7. When $\bar{\lambda}_{\text{p}}$ is larger, the strut behaves like a purely elastic strut and the ultimate load is principally governed by its elastic behaviour. As has been demonstrated in [20], the tangent flexural stiffness of an elastic strut with doubly-symmetric imperfections (case 4) is smaller than that of a strut with mono-symmetric imperfections (case 2). Therefore, the corresponding ultimate load for struts with doubly-symmetric imperfections is lower than that with mono-symmetric ones. When $\bar{\lambda}_{\text{p}}$ is smaller, the ultimate state of struts is principally governed by material failure. The mono-symmetric imperfections introduce an additional eccentricity to the strut, which facilitates the material failure within the more compressed web.

Under the same local buckling energy level due to imperfections, the mono-symmetric

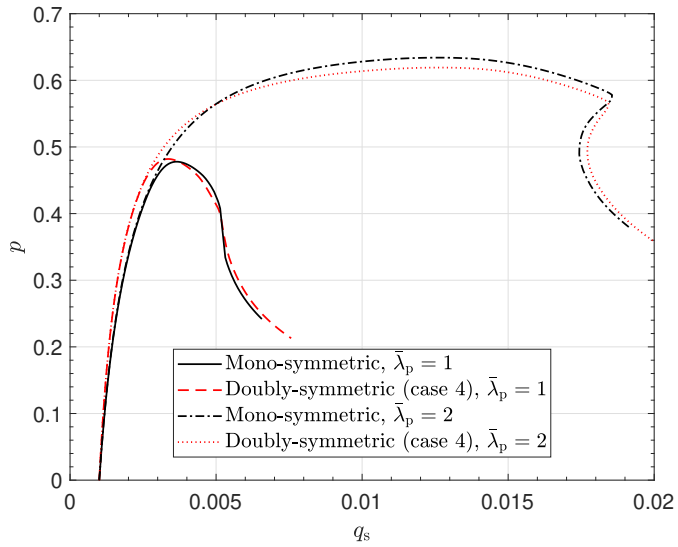

Figure 7: Equilibrium path of long length struts ($L = 4800$ mm) with the most severe mono-symmetric and doubly-symmetric periodic local imperfections at two different normalized slenderness levels.

imperfection is more severe than the doubly-symmetric one (case 3) at all $\bar{\lambda}_p$ levels investigated; the difference increasing with decreasing $\bar{\lambda}_p$. This is also attributed to the change in the aforementioned governing failure mode. As for cases 3 and 4, which have the same cross-section imperfection profiles but different local bending energy levels due to local imperfections, the corresponding wavelengths of the most severe imperfection profiles are very close. It implies that the wavelengths are insensitive to the imperfection amplitude, which is different from the purely elastic case [20]. Moreover, it should also be noted that a small increase or decrease in the value of β_i in the neighbourhood of $\beta_{i,\text{Worst}}$ only leads to a tiny change in the ultimate load (less than 0.5% in p_u for $\beta_{i,\text{Worst}} \pm 4$ for all cases investigated).

4.2. Effects of varying the degree of localization α_i

As described in the algorithm presented in Figure 4, the study on the effect of localization is based on the results of the immediately preceding section. The imperfection wavelength, *i.e.* the number of half-waves β_i, for each case is kept to the value corresponding to the lowest ultimate load, as presented in Table 4. The equivalent local bending energy due to local imperfections $U^0_{b,l}$ also remains the same in each case. In contrast with the relationship of A_{i0} versus β_i, the increase in α_i leads to an increase in A_{i0} under the constraint of equal local bending energy due to imperfections.

The relationship between the normalized ultimate load p_u and the degree of localization α_i for the four characteristic length struts at different yielding stress levels is presented in Figure 8. Initially, the ultimate load decreases with the imperfection profile changing from periodic to localized in all cases. Further increase of α_i subsequently leads to an increase in the ultimate load, even though the imperfection amplitude increases. This is

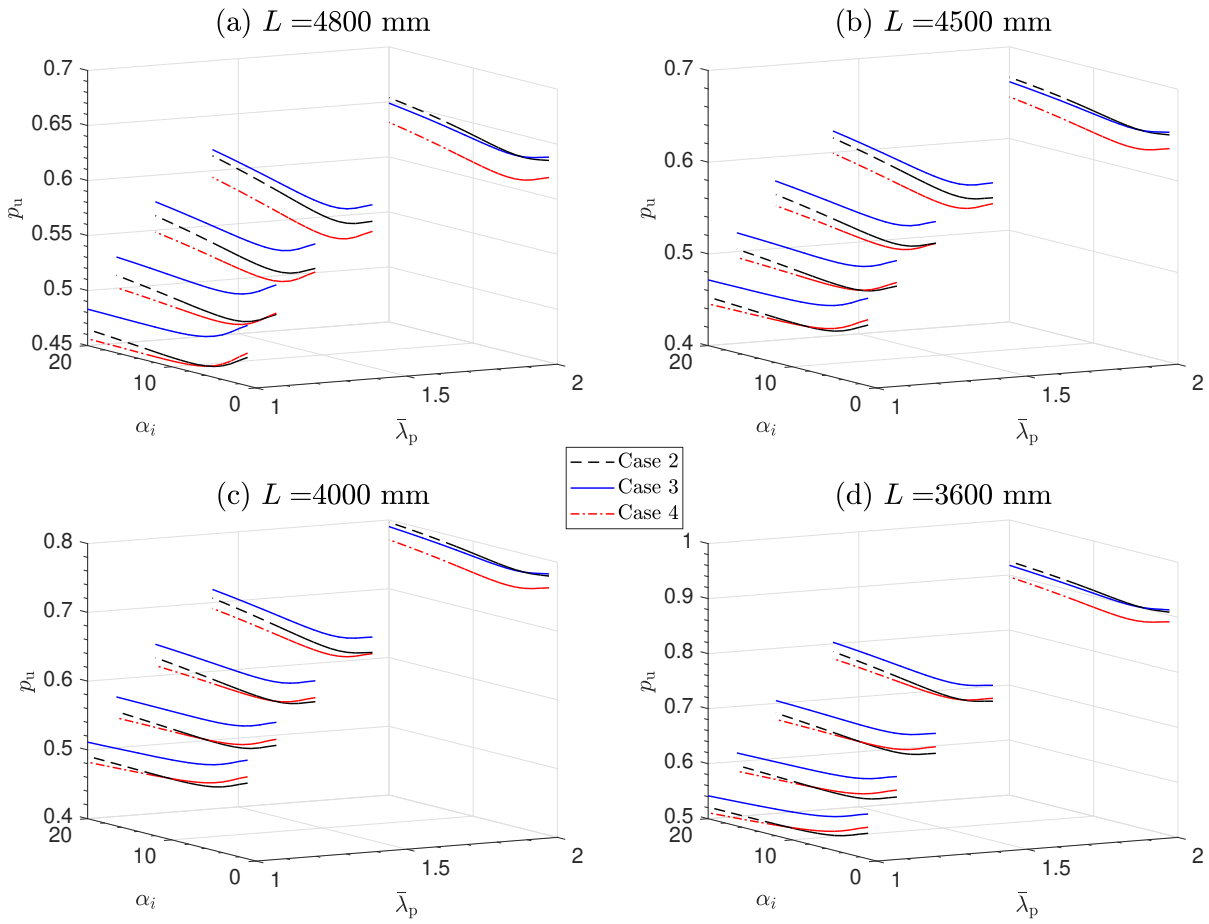

Figure 8: Normalized ultimate load $p_u = P_u/P^C$ versus the degree of imperfection localization α_i with different local imperfection cases presented in Table 3 for the four characteristic length struts with different cross-sectional local slenderness $\bar{\lambda}_p$ levels.

attributed to the fact that struts with highly localized imperfections exhibit a relatively higher tangent flexural stiffness than those with more periodic ones [20], thus leading to a higher ultimate load. It, again, demonstrates that the imperfection amplitude is insufficient as the sole criterion to determine the severity of geometric imperfections. However, for the intermediate and short length struts with doubly-symmetric imperfections, the further increase in α_i leads to a decrease in the ultimate load when $\bar{\lambda}_p$ is close to unity. As explained in §4.1, the ultimate state is principally governed by material failure in such cases. The highly localized imperfections with large amplitudes would definitely facilitate such a failure mode. For illustration purposes, the equilibrium paths of the intermediate length struts with the most severe doubly-symmetric imperfection profiles at $\bar{\lambda}_p = 1$ and 2 are presented in Figure 9. The equilibrium paths of the examples with the degrees of localization α_i being those of the most severe imperfection profile at two different levels of $\bar{\lambda}_p$ are also presented for comparison purposes. The strut with $\alpha_i = 20$ exhibits a higher

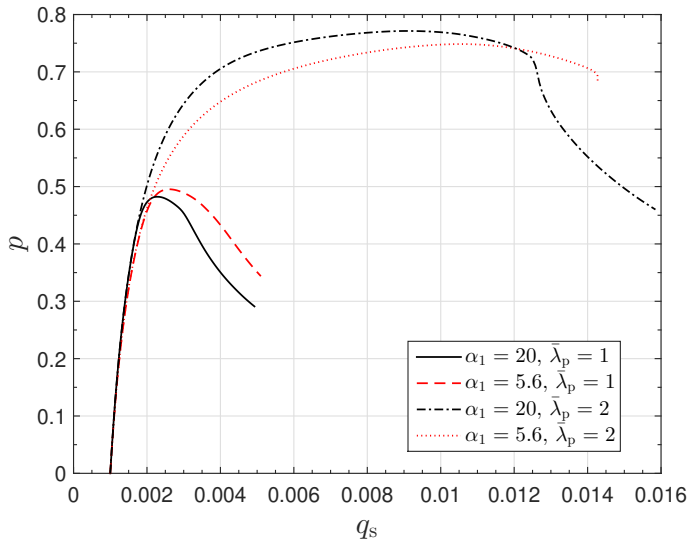

Figure 9: Equilibrium paths of intermediate length struts ($L = 4000$ mm) with doubly-symmetric cross-sectional imperfections (case 4) at different $\bar{\lambda}_p$ levels. Note that cases where $\alpha_1 = 20$ and 5.6 correspond to the degree of localization of the most severe imperfection profile at $\bar{\lambda}_p = 1$ and 2 respectively.

stiffness than that with $\alpha_i = 5.6$ for both $\bar{\lambda}_p$ levels. Since the strut failure is principally governed by the elastic behaviour when $\bar{\lambda}_p = 2$, the less localized imperfection is more severe. When $\bar{\lambda}_p = 1$, the failure of the strut is principally governed by material failure. The strut with $\alpha_i = 20$ exhibits a lower ultimate load than that with $\alpha_i = 5.6$ due to the material failure; the highly localized imperfection resembling the formation of a plastic hinge.

The ultimate load as well as the degree of imperfection localization and amplitude for struts with the most severe imperfection profiles for the four characteristic length struts at different cross-section slenderness levels are summarized in Table 5. In terms of the ultimate load, the difference between cases 2–4 compared with case 1 increases with decreasing $\bar{\lambda}_p$. Specifically, for the transitional length strut ($L = 4500$ mm) with doubly-symmetric imperfections (case 4), the difference increases from 6.7% at $\bar{\lambda}_p = 2$ to 13.2% at $\bar{\lambda}_p = 1$. Among all the four cases, the most severe case is always case 4 for various different strut lengths as well as local slenderness levels. This is different from the periodic imperfection cases presented in Table 4. In order to understand the effects of imperfection localization on the ultimate load more quantitatively, a comparison of the ultimate loads with the most severe localized and periodic imperfection profiles is presented in Table 6. It can be seen that the ultimate load erosion due to localization increases with decreasing $\bar{\lambda}_p$. Moreover, the load-carrying capacity erosion in the doubly-symmetric imperfections (cases 3 and 4) is relatively larger than that for mono-symmetric ones and the erosion in case 4 is the most significant amongst all three cases.

As for the most severe imperfection profile, the degree of localization α_i increases with decreasing $\bar{\lambda}_p$. The values of α_i for doubly-symmetric imperfections are generally higher

Table 5: Normalized ultimate load, degree of imperfection localization α_i and normalized local imperfection amplitude A_{0i}/t of the most severe imperfection profile at different cross-sectional local slenderness levels $\bar{\lambda}_{\mathrm{p}}$. Note that the rest of the table is as described in Table 4; the wavelengths of the modulated imperfection profiles are those presented in Table 4.

L	$\bar{\lambda}_{\mathrm{p}}$	$P_{\mathrm{u}}/P_{\mathrm{u,LBA,FE}}$ cases			α_i cases			A_{0i}/t cases		
(mm)		2	3	4	2	3	4	2	3	4
	1.000	0.923	0.972	**0.918**	7.525	10.828	10.788	0.997	0.847	1.227
	1.095	0.935	0.979	**0.926**	6.566	7.552	7.909	0.932	0.738	1.009
4800	1.225	0.949	0.983	**0.933**	5.606	6.241	6.566	0.863	0.645	0.921
	1.414	0.965	0.985	**0.939**	4.838	5.586	5.990	0.806	0.611	0.880
	2.000	0.983	0.983	**0.949**	3.879	4.931	5.414	0.675	0.553	0.805
	1.000	0.872	0.918	**0.868**	8.101	19.345	20.000	1.023	1.116	1.578
	1.095	0.886	0.930	**0.883**	6.566	8.207	8.677	0.923	0.731	1.045
4500	1.225	0.905	0.941	**0.895**	5.798	6.241	6.758	0.869	0.639	0.923
	1.414	0.929	0.951	**0.909**	5.030	5.586	5.990	0.812	0.606	0.871
	2.000	0.965	0.965	**0.933**	3.879	4.931	5.414	0.665	0.546	0.759
	1.000	0.911	0.954	**0.900**	9.636	20.000	20.000	1.144	1.162	1.620
	1.095	0.922	0.972	**0.922**	7.333	10.172	20.000	0.999	0.834	1.620
4000	1.225	0.935	0.978	**0.933**	5.990	6.897	7.717	0.905	0.688	1.014
	1.414	0.952	0.980	**0.940**	5.222	6.241	6.182	0.809	0.624	0.865
	2.000	0.979	0.978	**0.947**	4.071	4.931	5.606	0.689	0.530	0.785
	1.000	0.908	0.944	**0.890**	14.051	20.000	20.000	1.356	1.141	1.590
	1.095	0.918	0.962	**0.910**	8.293	20.000	20.000	1.045	1.141	1.590
3600	1.225	0.933	0.975	**0.929**	6.374	8.207	9.444	0.918	0.737	1.101
	1.414	0.945	0.978	**0.942**	5.414	6.241	6.758	0.849	0.644	0.883
	2.000	0.976	0.975	**0.947**	4.071	5.586	5.798	0.672	0.578	0.776

than those for mono-symmetric ones. As aforementioned, the imperfection amplitude increases with α_i under the constraint of equal local bending energy due to imperfections $U^0_{\mathrm{b},li}$. Apart from struts with $\bar{\lambda}_{\mathrm{p}} = 2$ and doubly-symmetric imperfections (case 3), the amplitudes of the most severe imperfection are all much larger than that for case 1, *i.e.* the tolerance level value $A_{i0}/t = 0.6$. For illustration purposes, the longitudinal components of the most severe imperfection profile for intermediate length struts with cases 2 and 4 at selected cross-section slenderness levels as well as the imperfection for case 1 are shown in Figure 10.

4.3. Local imperfections constrained to manufacturing tolerance level

Based on the algorithm presented in Figure 4, the effects of varying the imperfection profile on the erosion of load-carrying capacity have been investigated and the most severe profiles for each cases have been determined. However, it should be noted that the amplitudes of the most severe imperfection profiles presented in Table 5 exceed the recommended local imperfection tolerance [59]. Since manufacturers principally adopt the tolerance level

Table 6: Comparison of the ultimate load for the four characteristic length struts with the most severe localized and periodic imperfection profiles at different cross-section slenderness levels.

	$P_{\mathrm{u},\alpha_{i,\mathrm{Worst}}}/P_{\mathrm{u},\alpha_i=0}$									
$\bar{\lambda}_{\mathrm{p}}$	1.000	1.095	1.225	1.414	2.000	1.000	1.095	1.225	1.414	2.000
L (mm)			4800					4500		
Case 2	0.958	0.967	0.976	0.984	0.994	0.956	0.966	0.976	0.984	0.994
Case 3	0.951	0.962	0.972	0.980	0.989	0.948	0.962	0.972	0.980	0.990
Case 4	0.945	0.955	0.964	0.971	0.983	0.939	0.955	0.965	0.972	0.984
L (mm)			4000					3600		
Case 2	0.953	0.964	0.974	0.983	0.994	0.949	0.962	0.973	0.982	0.994
Case 3	0.937	0.959	0.972	0.980	0.989	0.928	0.950	0.970	0.980	0.989
Case 4	0.924	0.948	0.963	0.972	0.983	0.912	0.934	0.960	0.972	0.983

of imperfection amplitude as the quality control, the determined worst profiles with excessive amplitudes would not be practically significant. Therefore, based on the algorithm presented in Figure 4, the most severe imperfection profile under the constraint of imperfection tolerance is investigated. A summary of the results is presented in Table 7. With the decrease of the imperfection amplitude, alongside the degree of localization, the corresponding ultimate load increases. The most severe imperfection profiles amongst cases 2–4 at different strut lengths as well as cross-sectional slenderness levels are almost the same as that in the purely periodic case, as presented in Table 4. Specifically, case 4 is the most severe for long length struts and those with high $\bar{\lambda}_{\mathrm{p}}$ levels, where the failure is principally governed by elastic behaviour; case 2 is the most severe for struts with local buckling being critical and with low $\bar{\lambda}_{\mathrm{p}}$ levels, where the failure is governed by material failure. The values of α_i for cases 2 and 4 are much smaller than those presented in Table 5, which do not include the imperfection tolerance constraint. The imperfection amplitudes of the most severe profiles for all cases are equal to the tolerance level value except for struts with a doubly-symmetric imperfection (case 3) and $\bar{\lambda}_{\mathrm{p}} = 2$. Moreover, since case 3 corresponds to a lower level of local bending energy due to the imperfection when compared with case 4, with the same imperfection amplitude as case 4, it leads to much larger values of α_i.

4.4. Periodic approximation for most severe imperfection

The process of determining the most severe imperfection profile based on the algorithm presented in Figure 4 is complex and cumbersome to some degree. Moreover, the determined most severe imperfection profiles, *i.e.* the modulated longitudinal and mono-symmetric cross-sectional components, are not convenient to model. Therefore, it would be advantageous if the most severe imperfection profile could be approximated using the profiles with periodic longitudinal and doubly-symmetric components, which could be obtained directly from some existing software, such as CUFSM [60] and Abaqus [40]. Figure 11 presents the comparison between the ultimate loads with the most severe imperfection profile from cases 2 and 4 alongside those using the approximate periodic imperfection profiles with the doubly-symmetric cross-sectional component. It should be stressed that

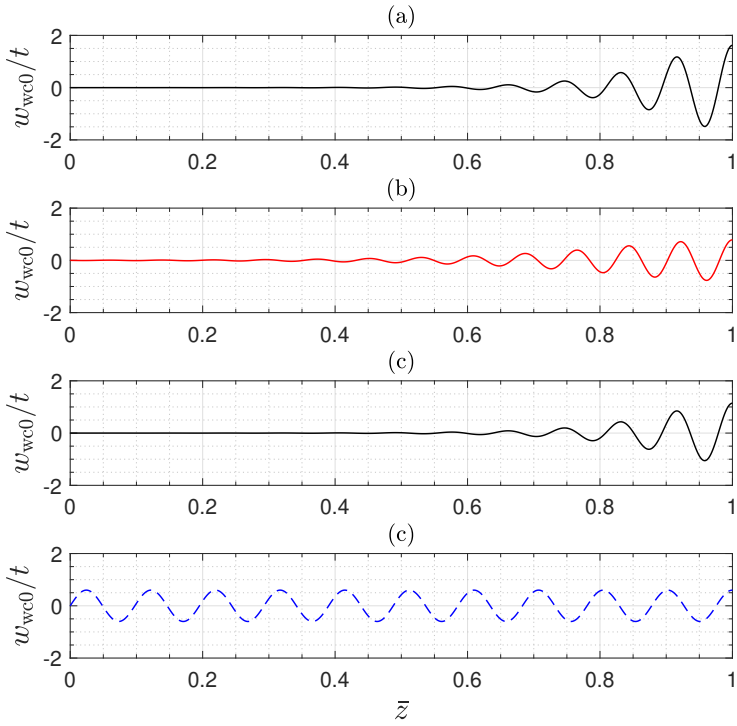

Figure 10: Longitudinal component of local imperfection profiles for intermediate length struts ($L = 4000$ mm). Most severe doubly-symmetric imperfections (case 4) with (a) $\bar{\lambda}_p = 1$ and (b) $\bar{\lambda}_p = 2$; (c) most severe mono-symmetric imperfection with $\bar{\lambda}_p = 1$; (d) periodic imperfection with the wavelength being the same as that of the local eigenmode with the lowest load and at the tolerance level $A_0 = d/200 = 0.6t$. Note that $\bar{z} = 2z/L$ and the imperfection profile is symmetric about $\bar{z} = 1$.

the wavelengths of the 'approximate' periodic imperfection profile are the same as those of case 4 presented in Table 4 and the amplitudes are equal to the tolerance value, *i.e.* $A_0 = d/200$. It can be seen that the 'approximate' imperfection profile can generally provide a reasonably accurate estimation of the response from the most severe imperfection profile in terms of the ultimate load. Specifically, the average ratio of the ultimate load of struts with the most severe imperfection profile (the more severe cases between cases 2 and 4) and the approximate ones is 1.001 and the coefficient of variation (COV) is 0.98%. The approximation leads to a slight overestimate in the ultimate load prediction for struts with $\bar{\lambda}_p$ being close to unity and local buckling being critical; the error is within 2% and decreases with the increase of the strut length as well as the cross-sectional slenderness $\bar{\lambda}_p$. For struts with a relatively large cross-sectional slenderness, the 'approximate' periodic imperfection would lead to a safe, yet accurate, prediction of the ultimate load. This is reasonable since the most severe imperfection profile in such cases is modulated with doubly-symmetric cross-sectional components and a small degree of localization.

For illustration purposes, the 'approximate' periodic and the actual most severe imperfection profiles for two typical cases are presented in Figure 12. In both cases, the

Table 7: Normalized ultimate load, degree of imperfection localization and local imperfection amplitude of the most severe imperfection profile at different cross-sectional local slenderness levels under the constraint of equal local bending energy alongside the local imperfection amplitude tolerance. Note that the ultimate loads are normalized with respect to case 1, where the linear buckling mode is introduced as the geometric imperfection with the amplitude being $A_{i0}/t = 0.6$ for all cases unless specified (*e.g.* case 3, $\bar{\lambda}_{\mathrm{p}} = 2.0$); the wavelengths of the modulated imperfection profiles are those presented in Table 4.

L (mm)	$\bar{\lambda}_{\mathrm{p}}$	$P_{\mathrm{u}}/P_{\mathrm{u,LBA,FE}}$ cases			α_i cases			A_{0i}/t cases		
		2	3	4	2	3	4	2	3	4
4800	1.000	**0.948**	0.981	0.958	2.162	5.371	1.899	0.6	0.6	0.6
	1.095	0.954	0.984	**0.953**	2.162	4.915	2.270			
	1.225	0.962	0.984	**0.953**	2.162	5.371	2.270			
	1.414	0.972	0.985	**0.954**	2.162	5.371	2.270			
	2.000	0.984	0.983	**0.956**	2.834	4.931	2.625		0.553	
4500	1.000	**0.897**	0.929	0.906	2.251	5.478	2.365	0.6	0.6	0.6
	1.095	**0.904**	0.934	0.908	2.251	5.478	2.365			
	1.225	0.917	0.941	**0.914**	2.251	5.478	2.365			
	1.414	0.936	0.951	**0.923**	2.251	5.478	2.365			
	2.000	0.965	0.965	**0.937**	2.964	4.931	3.119		0.546	
4000	1.000	**0.943**	0.978	0.958	2.026	5.190	2.118	0.6	0.6	0.6
	1.095	**0.944**	0.979	0.958	2.026	5.190	2.118			
	1.225	**0.950**	0.980	0.957	2.026	5.190	2.121			
	1.414	0.959	0.980	**0.953**	2.435	5.763	2.555			
	2.000	0.979	0.978	**0.952**	2.837	4.931	2.976		0.530	
3600	1.000	**0.942**	0.976	0.959	2.166	5.380	2.270	0.6	0.6	0.6
	1.095	**0.942**	0.978	0.959	2.166	5.380	2.270			
	1.225	**0.944**	0.979	0.959	2.166	5.380	2.270			
	1.414	**0.954**	0.979	0.955	2.166	5.380	2.742			
	2.000	0.977	0.975	**0.952**	3.059	5.586	3.211		0.578	

initial deformation of the approximate imperfection profile is larger than the actual most severe imperfection. In particular, it should be noted that the difference is even larger for the imperfection with mono-symmetric cross-sectional components since the cross-section component of the approximate most severe imperfection is doubly-symmetric. However, as shown in Figure 11, the ultimate load of the short length struts with the most severe imperfection is lower than that of the 'approximate' imperfection with a larger deformation in both cross-sectional and longitudinal dimensions. For the long length strut, scaling the imperfection amplitude near the ends to the tolerance level value only leads to a further 1% drop in the load-carrying capacity. Therefore, it may be concluded that the severity of imperfections principally depends on the characteristic failure mode being triggered rather than the absolute deformation or the magnitude of local bending energy stored due to imperfections. This also lends support to the current methodology of determining the most severe imperfection profile based on equal local bending energy, since it can consider

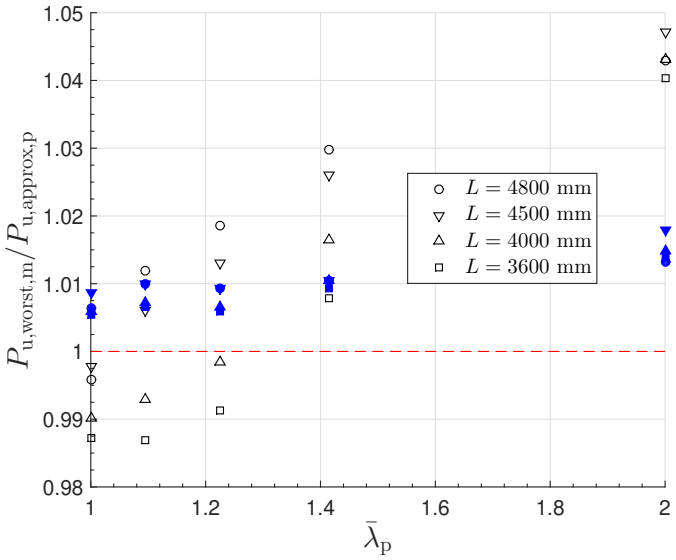

Figure 11: Comparison of ultimate loads with the most severe modulated imperfection profile (subscript m) and the 'approximate' periodic profiles (subscript p) at different cross-sectional slenderness levels. Hollow and solid symbols represent the most severe imperfection profile in cases 2 and 4 respectively. Note that the key parameters of the most severe imperfection profiles are presented in Table 7; wavelengths of the 'approximate' periodic imperfections are the same as those for case 4 presented in Table 4.

the variation of imperfection profiles in both cross-sectional as well as the longitudinal dimensions.

5. Parametric study

Hitherto, numerical results have shown that imperfection profiles with doubly-symmetric cross-section and periodic components can be used as a relatively accurate approximation of the most severe imperfection profile in terms of the ultimate load. Hence, a further parametric study is conducted to evaluate the effects of varying geometric properties as well as the material yielding stress levels on the wavelength of the most severe periodic imperfection profile with a doubly-symmetric cross-sectional component (case 4). The ultimate aim currently is to propose an explicit equation approximating the most severe local imperfection wavelength Λ_{Worst}. From Table 4, it can be seen that the value of $\Lambda_{\mathrm{Worst}}/\Lambda_{\mathrm{LBA}}$ ranges from 0.78 to 0.89. In order to make the solution process more efficient, an updated algorithm is adopted, which is presented in Figure 13. Instead of initiating the solution process from β_0 and finding the most severe case by increasing β_i, the updated algorithm first solves the ultimate load with the estimated most severe imperfection profile β_{M} as well as two neighbouring profiles with $\beta_{\mathrm{L}} = \beta_{\mathrm{M}} - 2$ and $\beta_{\mathrm{U}} = \beta_{\mathrm{M}} + 2$. The following solution steps are determined based on the relative magnitude of the ultimate loads for a given value of β_i, *i.e.* $P_{\mathrm{u}}(\beta_{\mathrm{M}})$, $P_{\mathrm{u}}(\beta_{\mathrm{L}})$ and $P_{\mathrm{u}}(\beta_{\mathrm{U}})$. In the current study, the initial β_{M} is determined based on the estimation that $\Lambda^{\mathrm{est}}_{\mathrm{Worst}} = 0.85\Lambda_{\mathrm{LBA}}$ and an adjustment is made, if necessary,

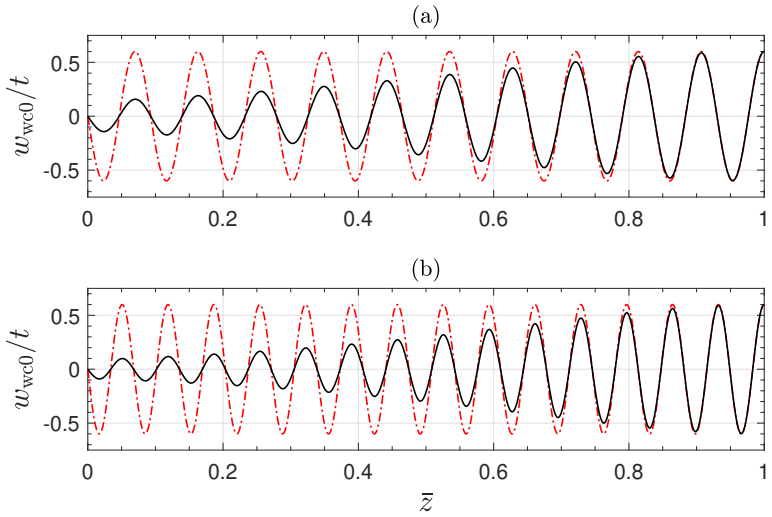

Figure 12: Visual comparison of the approximate (dot-dashed line) and actual most severe (solid line) imperfection profiles. (a) Short length strut (L = 3600 mm) with mono-symmetric imperfection and $\bar{\lambda}_{\mathrm{p}} = 1$. (b) Long length strut (L = 4800 mm) with doubly-symmetric imperfection (case 4) and $\bar{\lambda}_{\mathrm{p}} = 2$.

to ensure that β_{M} is an odd integer such that the boundary conditions are satisfied. From the results, it generally takes a maximum of 2 complete iterations to obtain the solution, *i.e.* 5 GMNIAs in total. Moreover, since Table 4 has shown that β_{Worst} for struts with different yielding stress levels ($\bar{\lambda}_{\mathrm{p}}$) are very close, the solved β_{Worst} in the current case is used as the initial β_{M} estimate for the proceeding case to improve efficiency.

The principal parameters and their ranges are presented in Table 8. Figure 14 presents

Table 8: Principal parameters and their ranges for the parametric study. Note that the critical buckling load ratio is altered by varying the strut length and the cross-sectional slenderness is altered by varying the material yielding stress levels.

Principal parameters	Range
Cross-section aspect ratio d/b	$1 \rightarrow 2.5$
Critical buckling load ratio $P_{\mathrm{o}}^{\mathrm{C}}/P_{\mathrm{l}}^{\mathrm{C}}$	$0.9 \rightarrow 4$
Cross-sectional slenderness $\bar{\lambda}_{\mathrm{p}}$	$1 \rightarrow 2$
Plate width–thickness ratio d/t	$60 \rightarrow 150$

the effects of varying the cross-section aspect ratio and the strut length on the most severe imperfection wavelength for different cross-sectional slenderness values, where the plate width–thickness ratio is fixed to 120. It can be seen that the values of $\Lambda_{\mathrm{Worst}}/\Lambda_{\mathrm{LBA}}$ are fairly constant with (a) varying d/b and (b) $P_{\mathrm{o}}^{\mathrm{C}}/P_{\mathrm{l}}^{\mathrm{C}}$. Hence, it may be concluded that the effects of geometric properties on the most severe periodic imperfection profile are not significant. Therefore, a relationship to describe the most severe wavelength Λ_{Worst} and the

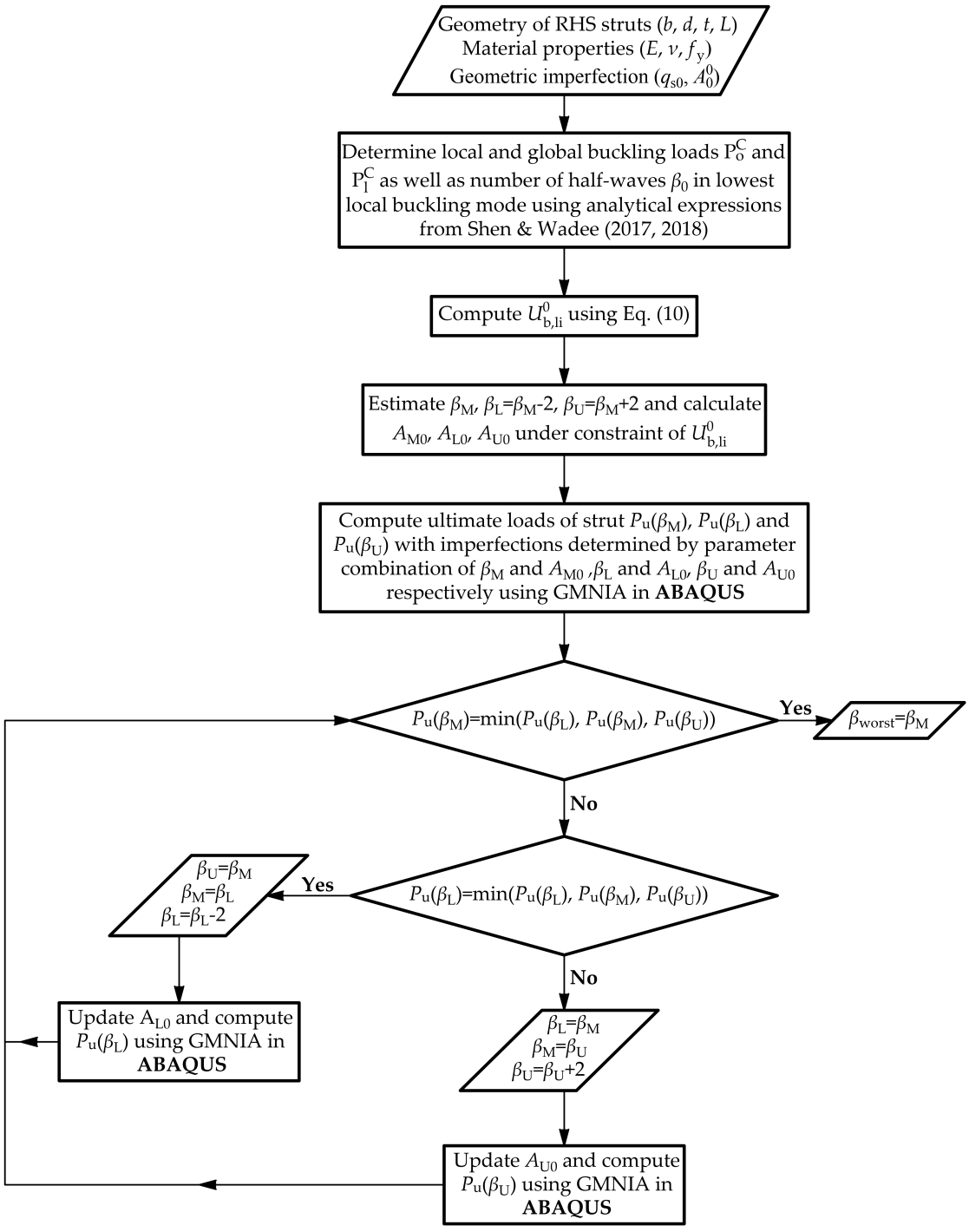

Figure 13: Algorithm for the parametric studies to determine the effects of varying geometric properties as well as material yielding stress levels on the wavelength of the most severe periodic local imperfections under the constraint of the equal local bending energy compared to the initial case with $\beta_i = \beta_0$, $A_{i0} = A_{i0}^0$ and $U_{b,1i}^0$.

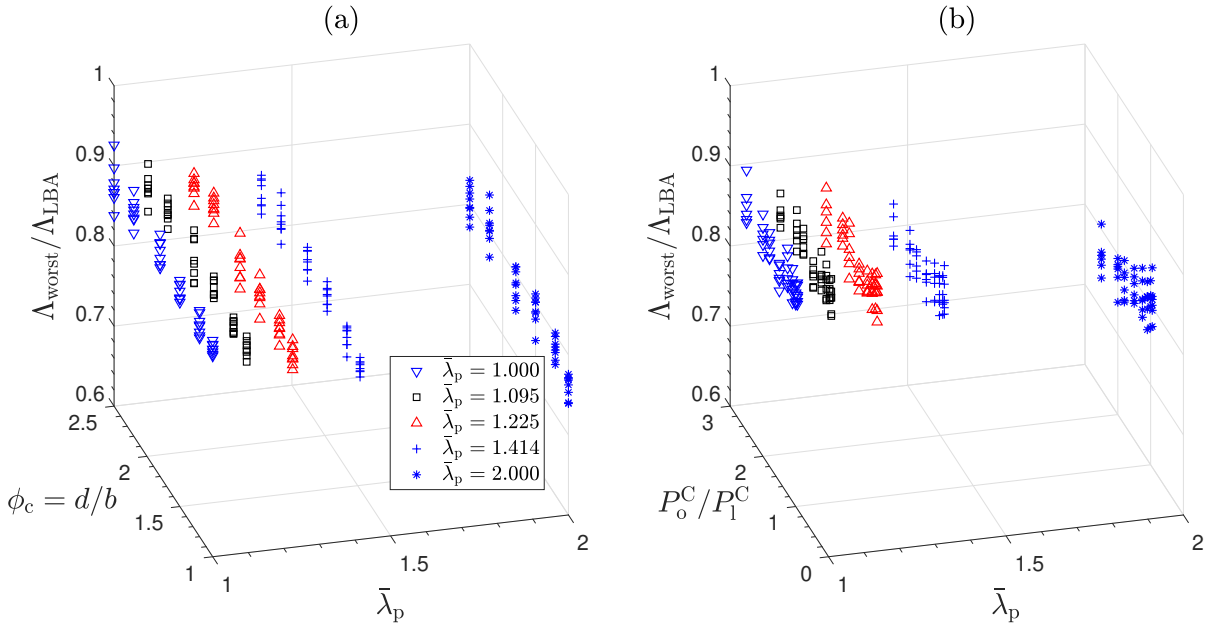

Figure 14: Effects of (a) cross-section aspect ratio and (b) strut length on the wavelength of the most severe periodic imperfections. Note that the ratio d/t is fixed to 120 in these graphs.

normalized cross-sectional slenderness $\bar{\lambda}_{\mathrm{p}}$ is fitted initially for the ratio where $d/t = 120$:

$$\frac{\Lambda_{\mathrm{Worst}}}{\Lambda_{\mathrm{LBA}}} = \frac{1}{3} + 0.708 \tanh(\bar{\lambda}_{\mathrm{p}}^{-1/5}) \tag{12}$$

and a further parametric study was conducted with three additional d/t ratios. The average and COV of the ratio of Eq. (12) to the FE results for the example struts considered are presented in Table 9. The comparisons with the corresponding number of half-waves β_{Worst}

Table 9: Average and COV of proposed Eq. (12) to FE results ratio for all d/t ratios considered.

d/t	Average	COV
60	0.967	4.51%
80	0.986	3.24%
120	0.996	2.26%
150	1.010	2.14%
All combined	0.992	3.24%

predicted by FE and Eq. (12) are shown in Figure 15, which show very good correlation in each case presented. Figure 16 presents the distribution of the difference between $\beta_{\mathrm{Worst,FE}}$ and $\beta_{\mathrm{Worst,Eq}}$ for various d/t ratios. As demonstrated in Figure 6, a small increase or decrease in the value of β in the neighbourhood of β_{Worst} only leads to a tiny change in the ultimate load. Therefore, it may be concluded that the wavelength of the most severe

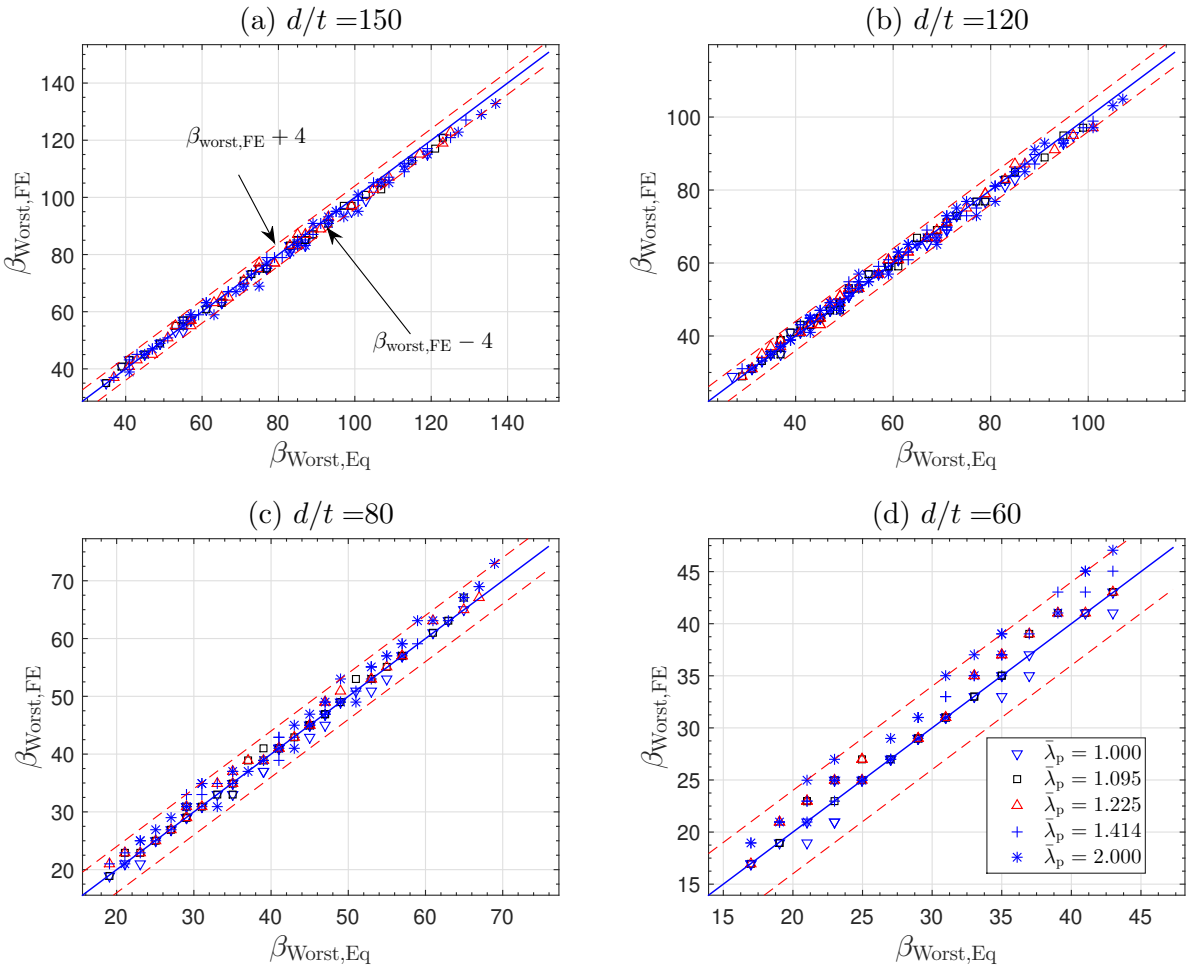

Figure 15: Comparison of the number of half-waves in the most severe periodic imperfection profile solved using GMNIA in ABAQUS and the proposed fitting equation. The upper and lower dashed lines in (b–d) represent $\beta_{\text{Worst,FE}} + 4$ and $\beta_{\text{Worst,FE}} - 4$ as labelled in (a); the solid line represents $\beta_{\text{Worst,FE}} = \beta_{\text{Worst,Eq}}$.

periodic imperfection profile is principally related to the material yielding stress and Eq. (12) provides a relatively accurate approximation of the most severe imperfection profile for RHS struts within the parametric range presented in Table 8.

6. Concluding remarks

A nonlinear FE model developed within the commercial package ABAQUS for inelastic thin-walled rectangular hollow section struts susceptible to local–global mode interaction with bespoke local and global imperfection profiles was used to investigate the effects of different local imperfection profiles on the load-carrying capacity. Using a unified local imperfection measurement based on the concept of equal local bending energy, the effects of imperfection profiles, *i.e.* the cross-section profile, the wavelength and the degree of

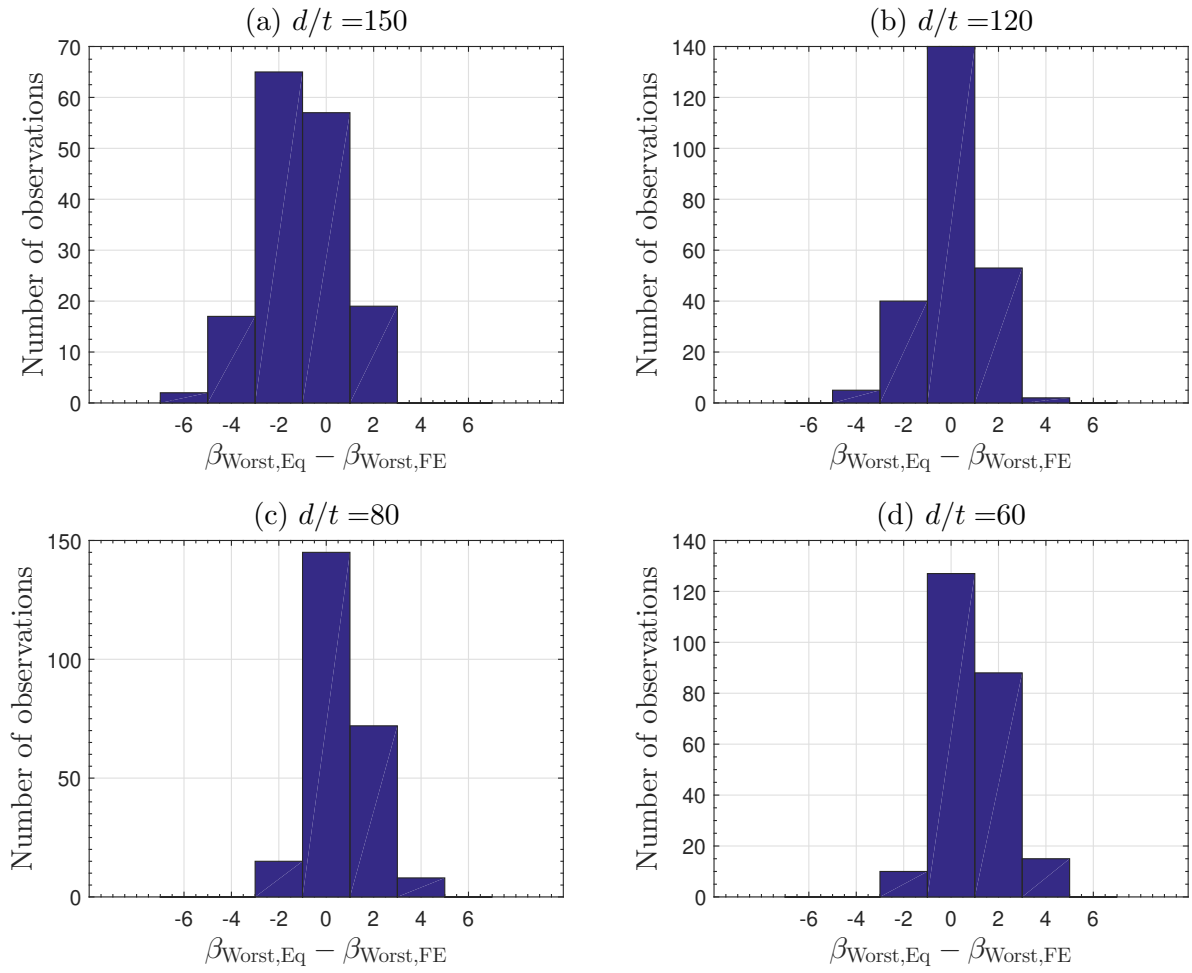

Figure 16: Distribution of differences in β_{Worst} between Eq. (12) and the FE results. Note that $\beta_{\text{Worst,Eq}}$ slightly underestimates $\beta_{\text{Worst,FE}}$ for higher d/t ratios and this becomes a slight overestimation for the lower d/t ratios presented.

localization in the longitudinal direction, on the ultimate load and equilibrium behaviour were investigated for four characteristic length struts at different yielding stress levels. The most severe local imperfection profiles for example struts with different lengths and cross-sectional slenderness levels have been determined within the chosen cross-section and longitudinal imperfection parametric spaces. Subsequently, a systematic parametric study was conducted for wider geometric and material parameter spaces. An explicit expression to approximate the wavelength of the most severe periodic imperfection profile has been proposed based on the results from the parametric study and this compares excellently with the FE results of the investigated struts.

Based on the current findings, the following detailed conclusions may be drawn:

1. In terms of the imperfection cross-section profile, the mono-symmetric imperfection is more severe than the doubly-symmetric one under the same equal local bending

energy due to imperfections $U^0_{\mathrm{b},li}$. However, under the same initial imperfection amplitude A^0_0 and number of half-waves β^0_0, the severity of the mono- and doubly-symmetric imperfections depends on the cross-sectional local slenderness ($\bar{\lambda}_{\mathrm{p}}$) as well as the ratio of the global to local buckling load $P^{\mathrm{C}}_{\mathrm{o}}/P^{\mathrm{C}}_{\mathrm{l}}$, the latter being related to the strut length. The mono-symmetric imperfections are more severe in cases where local buckling is critical ($P^{\mathrm{C}}_{\mathrm{o}}/P^{\mathrm{C}}_{\mathrm{l}} > 1$) and $\bar{\lambda}_{\mathrm{p}}$ is small. In such cases, strut failure is principally governed by the mono-symmetric imperfection and the material. For cases where global buckling is critical $P^{\mathrm{C}}_{\mathrm{o}}/P^{\mathrm{C}}_{\mathrm{l}} < 1$ and $\bar{\lambda}_{\mathrm{p}}$ is relatively large, doubly-symmetric imperfections are more severe due to the large erosion in the tangent flexural stiffness [20]. The failure of such struts is principally governed by the erosion of the elastic post-buckling stiffness.

2. In terms of the effects of the number of half-waves β_i in the longitudinal direction of the imperfection profile, the increase in β_i from β_0 initially leads to a decrease in the ultimate load, even though the corresponding imperfection amplitude decreases under the constraint of equal $U^0_{\mathrm{b},li}$. However, the further increase in β_i leads to an increase in the ultimate load owing to the fact that the imperfection begins to correspond to a higher local eigenmode.
3. The influence of the degree of imperfection localization α_i on the ultimate load is related to the value of $\bar{\lambda}_{\mathrm{p}}$, $P^{\mathrm{C}}_{\mathrm{o}}/P^{\mathrm{C}}_{\mathrm{l}}$, alongside the imperfect cross-section profile. When $\bar{\lambda}_{\mathrm{p}}$ is large, the ultimate load initially decreases and then increases with the increase of α_i. This is attributed to the fact that the struts with large α_i correspond to a higher level of tangent stiffness in the struts, which leads to a higher ultimate load that is related to the elastic post-buckling stiffness [20]. When $\bar{\lambda}_{\mathrm{p}}$ is small, local buckling is critical and the imperfection cross-section profile is doubly-symmetric, the increase in α_i leads to a monotonic decrease in the ultimate load. This is attributed to the fact that the high degree of localization would lead to material failure first. However, in such cases, the imperfection amplitude is always larger than the tolerance level and is hence of limited practical significance.
4. Even though the most severe imperfection profiles determined based on the constraint of equal initial local bending energy correspond to one with mono-symmetric cross-sectional and modulated longitudinal components, it has been demonstrated currently that it can be approximated using imperfections with doubly-symmetric cross-sectional and periodic longitudinal components in terms of estimating the ultimate load of struts with good accuracy. This can simplify the analysis considerably.

Generally, it has been demonstrated that the local imperfection amplitude cannot be used as the sole measure of the severity of imperfections and the local eigenmode with the lowest load may not represent the most severe imperfection profile. The proposed imperfection measurement method and the solution algorithms provide systematic and consistent approaches to determine the effects of different imperfection profiles on the ultimate load of RHS struts. The methodology can be extended to investigate the effects of imperfection profiles on thin-walled members with other cross-section profiles [61, 62], particularly where mode interaction is a significant factor and the post-buckling profile

changes qualitatively while loading is continued.

Acknowledgement

Financial support for Jiajia Shen was provided by the President's PhD Scholarship scheme from Imperial College London.

References

[1] M. Ashby, Materials Selection in Mechanical Design (4th Edition), Butterworth-Heinemann, Oxford, 2011.

[2] N. S. Trahair, M. A. Bradford, D. A. Nethercot, L. Gardner, The behaviour and design of steel structures to EC3, CRC Press, 2007.

[3] C. Yu (Ed.), Recent Trends in Cold-Formed Steel Construction, Woodhead Publishing, 2016.

[4] V. Gioncu, General theory of coupled instabilities, Thin-Walled Struct. 19 (2) (1994) 81–127.

[5] J. M. T. Thompson, G. W. Hunt, A general theory of elastic stability, Wiley, London, 1973.

[6] J. Becque, K. J. R. Rasmussen, Experimental investigation of the interaction of local and overall buckling of stainless steel I-columns, ASCE J. Struct. Eng. 135 (11) (2009) 1340–1348.

[7] P. B. Dinis, D. Camotim, Post-buckling behaviour and strength of cold-formed steel lipped channel columns experiencing distortional/global interaction, Comput. Struct. 89 (34) (2011) 422–434.

[8] M. A. Wadee, L. Gardner, Cellular buckling from mode interaction in I-beams under uniform bending, Proc. R. Soc. A 468 (2137) (2012) 245–268.

[9] M. A. Wadee, L. Bai, Cellular buckling in I-section struts, Thin-Walled Struct. 81 (2014) 89–100.

[10] M. A. Wadee, M. Farsi, Cellular buckling in stiffened plates, Proc. R. Soc. A 470 (2168) (2014) 20140094.

[11] V. Gioncu, Elasto-plastic buckling of compression members as a coupled instability, Thin-Walled Struct. 19 (24) (1994) 221–235.

[12] L. Gardner, D. A. Nethercot, Experiments on stainless steel hollow sections – Part 2: Member behaviour of columns and beams, J. Constr. Steel. Res. 60 (9) (2004) 1319–1332.

[13] H. Degée, A. Detzel, U. Kuhlmann, Interaction of global and local buckling in welded RHS compression members, J. Constr. Steel. Res. 64 (7) (2008) 755–765.

[14] L. Pavlovčič, B. Froschmeier, U. Kuhlmann, D. Beg, Slender thin-walled box columns subjected to compression and bending, J. Civ. Eng. Manag. 16 (2) (2010) 179–188.

[15] H. X. Yuan, Y. Q. Wang, L. Gardner, Y. J. Shi, Local-overall interactive buckling of welded stainless steel box section compression members, Eng. Struct. 67 (2014) 62–76.

[16] L. Yang, G. Shi, M. Zhao, W. Zhou, Research on interactive buckling behavior of welded steel box-section columns, Thin-Walled Struct. 115 (2017) 34–47.

[17] N. Schillo, M. Feldmann, Interaction of local and global buckling of box sections made of high strength steel, Thin-Walled Struct. 128 (2018) 126–140.

[18] J. Loughlan, N. Yidris, P. R. Cunningham, The effects of local buckling and material yielding on the axial stiffness and failure of uniformly compressed I-section and box-section struts, Thin-Walled Struct. 49 (2) (2011) 264–279.

[19] J. Becque, Local-overall interaction buckling of inelastic columns: A numerical study of the inelastic Van der Neut column, Thin-Walled Struct. 81 (2014) 101–107.

[20] J. Shen, M. A. Wadee, Sensitivity of elastic thin-walled rectangular hollow section struts to manufacturing tolerance level imperfections, Eng. Struct. 170 (2018) 146–166.

[21] A. van der Neut, The interaction of local buckling and column failure of thin-walled compression members, in: Proceedings of the 12th International Congress on Applied Mechanics, Springer, 1969, pp. 389–399.

[22] H. Degée, N. Boissonnade, B. Rossi, Local and interactive post-buckling of RHS thin-walled members–comparing a new special beam finite element with shell FE models, Int. J. Struct. Stab. Dyn. 7 (02) (2007) 213–241.

[23] B. W. Schafer, Z. Li, C. D. Moen, Computational modeling of cold-formed steel, Thin-Walled Struct. 48 (10) (2010) 752–762.

[24] B. W. Schafer, T. Peköz, Computational modeling of cold-formed steel: characterizing geometric imperfections and residual stresses, J. Constr. Steel. Res. 47 (3) (1998) 193–210.

[25] R. B. Cruise, L. Gardner, Measurement and prediction of geometric imperfections in structural stainless steel members, Struct. Eng. Mech. 24 (1) (2006) 63–89.

[26] L. Pavlovčič, B. Froschmeier, U. Kuhlmann, D. Beg, Finite element simulation of slender thin-walled box columns by implementing real initial conditions, Adv. Eng. Softw. 44 (1) (2012) 63–74.

[27] Y. Ueda, T. Yao, The influence of complex initial deflection modes on the behaviour and ultimate strength of rectangular plates in compression, J. Constr. Steel. Res. 5 (4) (1985) 265–302.

[28] D. Dubina, V. Ungureanu, Effect of imperfections on numerical simulation of instability behaviour of cold-formed steel members, Thin-Walled Struct. 40 (3) (2002) 239–262.

[29] J. Bonada, M. Casafont, F. Roure, M. Pastor, Selection of the initial geometrical imperfection in nonlinear FE analysis of cold-formed steel rack columns, Thin-Walled Structures 51 (2012) 99–111.

[30] L. Bai, M. A. Wadee, Imperfection sensitivity of thin-walled I-section struts susceptible to cellular buckling, Int. J. Mech. Sci. 104 (2015) 162–173.

[31] E. L. Liu, M. A. Wadee, Mode interaction in perfect and imperfect thin-walled I-section struts susceptible to global buckling about the strong axis, Thin-Walled Struct. 106 (2016) 228–243.

[32] V. M. Zeinoddini, B. W. Schafer, Simulation of geometric imperfections in cold-formed steel members using spectral representation approach, Thin-Walled Struct. 60 (2012) 105–117.

[33] A. N. Trouncer, K. J. R. Rasmussen, A rational procedure for modelling imperfections in advanced analysis of frames with locally unstable members, Thin-Walled Struct. 96 (2015) 183–201.

[34] A. T. Sarawit, Y. Kim, M. C. M. Bakker, T. Peköz, The finite element method for thin-walled members-applications, Thin-Walled Struct. 41 (2-3) (2003) 191–206.

[35] R. S. Dow, C. S. Smith, Effects of localized imperfections on compressive strength of long rectangular plates, J. Constr. Steel. Res. 4 (1) (1984) 51–76.

[36] Z. Sadovskỳ, A. P. Teixeira, C. G. Soares, Degradation of the compressive strength of rectangular plates due to initial deflection, Thin-Walled Struct. 43 (1) (2005) 65–82.

[37] R. M. Luís, M. Witkowska, C. G. Soares, Collapse behaviour of damaged panels with a dimple imperfection, in: ASME 2007 26th International Conference on Offshore Mechanics and Arctic Engineering, American Society of Mechanical Engineers, 2007, pp. 687–697.

[38] J. Shen, M. A. Wadee, Imperfection sensitivity of rectangular hollow section struts susceptible to interactive buckling, Int. J. Non-Linear Mech. 99 (2018) 112–130.

[39] J. Shen, M. A. Wadee, Behaviour and design of inelastic thin-walled rectangular hollow section struts susceptible to local–global mode interaction, Eng. Struct. Submitted. 2018.

[40] ABAQUS, Version 6.14, Dassault Systèmes, Providence RI, USA, 2014.

[41] J. Shen, M. A. Wadee, Length effects on interactive buckling in thin-walled rectangular hollow section struts, Thin-Walled Struct. 128 (2018) 152–170.

[42] J. H. Zhu, B. Young, Aluminum alloy tubular columnspart I: Finite element modeling and test verification, Thin-Walled Struct. 44 (9) (2006) 961–968.

[43] J. Shen, M. A. Wadee, A. J. Sadowski, Numerical study of interactive buckling in thin-walled section box columns under pure compression, in: D. Camotim, P. B. Dinis, S. L. Chan, C. M. Wang, R. Goncalves, N. Silvestre, C. Basaglia, A. Landesmann, R. Bebiano (Eds.), Proceedings of the 8th International Conference on Advances in Steel Structures (ICASS' 2015), 2015, paper number: 44.

[44] H. X. Shen, Ultimate capacity of welded box section columns with slender plate elements, Steel Compos. Struct. 13 (1) (2012) 15–33.

[45] ECCS. TC 8, Ultimate limit state calculation of sway frames with rigid joints, Tech. rep. (1984).

[46] X. Yun, L. Gardner, Stress-strain curves for hot-rolled steels, J. Constr. Steel. Res. 133 (Supplement C) (2017) 36–46.

[47] J. Shen, M. A. Wadee, A. J. Sadowski, Interactive buckling in long thin-walled rectangular hollow section struts, Int. J. Non-Linear Mech. 89 (2017) 43–58.

[48] G. W. Hunt, M. A. Wadee, Localization and mode interaction in sandwich structures, Proc. R. Soc. A 454 (1972) (1998) 1197–1216.

[49] M. A. Wadee, Effects of periodic and localized imperfections on struts on nonlinear foundations and compression sandwich panels, Int. J. Solids Struct. 37 (8) (2000) 1191–1209.

[50] M. A. Wadee, M. Farsi, Imperfection sensitivity and geometric effects in stiffened plates susceptible to cellular buckling, Structures 3 (2015) 172–186.

[51] M. K. Wadee, G. W. Hunt, A. I. M. Whiting, Asymptotic and Rayleigh–Ritz routes to localized buckling solutions in an elastic instability problem, Proc. R. Soc. A 453 (1965) (1997) 2085–2107.

[52] H. Wu, J. Yang, S. Kitipornchai, Imperfection sensitivity of postbuckling behaviour of functionally graded carbon nanotube-reinforced composite beams, Thin-Walled Struct. 108 (2016) 225–233.

[53] E. Riks, C. C. Rankin, F. A. Brogan, On the solution of mode jumping phenomena in thin-walled shell structures, Comput. Meth. Appl. Mech. Eng. 136 (12) (1996) 59–92.

[54] T. Usami, Y. Fukumoto, Welded box compression members, ASCE J. Struct. Eng. 110 (10) (1984) 2457–2470.

[55] Z. Sadovskỳ, J. Kriváček, V. Ivančo, A. Ďuricová, Computational modelling of geometric imperfections and buckling strength of cold-formed steel, J. Constr. Steel. Res. 78 (2012) 1–7.

[56] P. S. Bulson, The stability of flat plates, Chatto and Windus, London, UK, 1970.

[57] X. Zhao, M. Tootkaboni, B. W. Schafer, Development of a laser-based geometric imperfection measurement platform with application to cold-formed steel construction, Exp. Mech. 55 (9) (2015) 1779–1790.

[58] EN-1993-1-3:2006E, Eurocode 3: Design of steel structures part 1-3. General rules-Supplementary rules for cold-formed members and sheeting (2006).

[59] EN-1993-1-5:2006E, Eurocode 3: Design of steel structures part 1-5. Plated structural elements (2006).

[60] B. W. Schafer, CUFSM: elastic buckling analysis of thin-walled members by finite strip analysis, available from http://www.ce.jhu.edu/bschafer/cufsm/ (2006).

[61] L. Bai, M. A. Wadee, Slenderness effects in thin-walled I-section struts susceptible to local–global mode interaction, Eng. Struct. 124 (2016) 128–141.

[62] E. L. Liu, M. A. Wadee, Geometric factors affecting I-section struts experiencing local and strong-axis global buckling mode interaction, Thin-Walled Struct. 109 (2016) 319–331.